Journal of Energy Storage 55 (2022) 105802

Contents lists available at ScienceDirect

Journal of Energy Storage

journal homepage: www.elsevier.com/locate/est

Research papers

Thermodynamic investigation of latent-heat stores for pumped-thermal energy storage

Yao Zhao [a,b], Jian Song [b], Changying Zhao [c], Yongliang Zhao [d], Christos N. Markides [b,*]

[a] College of Smart Energy, Shanghai Jiao Tong University, Shanghai 200240, China
[b] Clean Energy Processes (CEP) Laboratory, Department of Chemical Engineering, Imperial College London, London SW7 2AZ, UK
[c] Institute of Engineering Thermophysics, School of Mechanical Engineering, Shanghai Jiao Tong University, Shanghai 200240, China
[d] State Key Laboratory of Multiphase Flow in Power Engineering, Xi'an Jiaotong University, Xi'an 710049, China

ARTICLE INFO

Keywords:
Cascaded latent-heat store
Joule-Brayton cycle
Liquid sensible-heat store
Packed-bed sensible-heat store
Pumped-thermal energy storage
Thermodynamic analysis

ABSTRACT

As a large-scale energy storage technology, pumped-thermal energy storage uses thermodynamic cycles and thermal stores to achieve energy storage and release. In this paper, we explore the thermodynamic feasibility and potential of exploiting cascaded latent-heat stores in Joule-Brayton cycle-based pumped-thermal energy storage systems. A thermodynamic model of cascaded latent-heat stores is developed, and the effects of the heat store arrangement (i.e., total stage number and stage area) and fluid velocity in the thermal store tubes as key parameters that affect the heat storage and release rates, as well as the roundtrip efficiency, are evaluated. A pure electricity-storage mode and a combined heating and power mode are proposed and investigated, which allows such technologies to transform from a pure electricity storage system to an energy management system supplying power and multi-grade thermal and cold energy, and also to integrate with external waste heat and/or cold sources. Results show that the roundtrip efficiency of cascaded latent-heat stores is higher in the combined heating and power mode than in the pure electricity-storage mode, and that roundtrip efficiencies ranging from 62 % to 100 % can be achieved in the combined heating and power mode, accompanied by a corresponding pressure loss gradient ranging from 10 Pa/m to 2270 Pa/m. A comparison with packed-bed and liquid sensible-heat stores is also performed, and the results indicate that if these can be well designed, cascaded latent-heat stores can deliver comparable performance in terms of the total heat storage and release rates, roundtrip efficiency and flow resistance loss. Therefore, it is concluded that cascaded latent-heat stores can be considered for use in Joule-Brayton cycle-based pumped-thermal energy storage systems aimed at intelligent energy management for the provision of power and multi-grade heat and cold, if the costs can justify this decision.

1. Introduction

Low-carbon and clean renewable energy technologies have gained increasing attention in recent decades, especially in solar and wind power sectors. Recently, renewables have dominated the growth in primary energy generation, which accounted for 5 % of all primary energy generation in 2018, and the share is expected to increase to between 20 % and 60 % by 2050 [1]. However, renewable energy represented by solar and wind power is associated with inevitable fluctuations in generation caused by climate, weather and other factors. Low-cost and large-scale energy storage is key to regulating the varying renewable energy output [2]. At present, there exist three main types of energy storage systems that could be deployed for large-scale storage: pumped-hydro energy storage (PHES), electrochemical energy storage (EES) and thermo-mechanical energy storage (TMES) [3].

PHES is cost-effective for large-scale energy storage, and accounts for over 95 % of the current global capacity, but it has restrictions that arise from particular geographical requirements [4]. EES includes a wide range of options, such as lead-acid, sodium-sulphur, lithium-ion and flow batteries, all of which have been attracting significant attention, leading to rapid performance improvements and cost reductions. At the same time, EES technologies still face challenges (e.g., limited lifetime, safety concerns, high costs) in the context of full commercialisation on a large scale [4]. Compressed-air energy storage (CAES), liquid-air energy storage (LAES) and pumped-thermal electricity/energy storage (PTES) are all TMES technologies. They have good projected thermodynamic performance, with roundtrip efficiencies (RTEs) above 60 %, long life

* Corresponding author.
E-mail address: c.markides@imperial.ac.uk (C.N. Markides).

https://doi.org/10.1016/j.est.2022.105802
Received 24 May 2022; Received in revised form 12 September 2022; Accepted 30 September 2022

Nomenclature

Abbreviations

PHES	pumped-hydro energy storage
EES	electrochemical energy storage
TMES	thermo-mechanical energy storage
CAES	compressed-air energy storage
LAES	liquid-air energy storage
PTES	pumped-thermal electricity/energy storage
RTE	roundtrip efficiency
TRL	technology readiness level
TES	thermal energy storage
PBSHS	packed-bed sensible-heat store
ORC	organic Rankine cycle
LSHS	liquid sensible-heat store
HTF	heat transfer fluid
CLHS	cascaded latent-heat store
PCM	phase change material
PES	pure electricity-storage
CHP	combined heating and power
NTU	number of transfer units
LMTD	average logarithmic mean temperature difference

Symbols

N	total stage number
A	heat transfer area (stage), m^2
T	temperature, K
D	diameter (shell side), m
d	diameter (tube side) or distance, m
W	width, m
p	pressure, Pa
$\dot{m}$	mass flow rate, kg/s
c_p	specific heat capacity, J/(kg·K)
k	thermal conductivity, W/(m·K)
Pr	Prandtl number
Δh	specific latent heat, J/kg
U	heat transfer coefficient, W/(m^2·K)
Q	heat transfer rate, W
C	parameter related to NTU
$\dot{E}x$	exergy transfer rate, W
$\dot{S}_g$	entropy generation rate, W/K
$\dot{S}_f$	entropy flow rate, W/K
s	specific entropy, J/(kg·K)
t	time, s
n	tube number
v	velocity, m/s
L	length of each stage, m
f	friction factor
h	convective heat transfer coefficient, W/(m^2·K)
Re	Reynolds number
Nu	Nusselt number
V	volume, m^3
j	Colburn factor
G	Lagrangian function or mass flux, kg/(s·m^2)
S_v	packing surface area per unit volume, m^{-1}
Ar	cross-section area, m^2

Greek symbols

ρ	density, kg/m^3
ξ	length-to-diameter ratio
η	volume design factor
τ	charging/discharging time, s
μ	dynamic viscosity, Pa·s
δ	Lagrange multiplier
θ	constant heat storage rate during charging, W
ε	porosity
φ	viscosity correction factor

Subscripts

m	melting
c	charging
d	discharging
i	the i-th stage
s	shell or solid
b	bundle
o	outer
i	inner
tp	tube pitch
e	environment
0	initial
in	inlet
out	outlet
f	fluid
heat	direct heating
tube	tube
PCM	phase change material
1	upper limit
2	lower limit
st	storage
re	release
tot	total
opt	optimal
cp	connection point
pd	packed bed
p	particle
ss	shell-side fluid
eff	effective
HX	heat exchanger
WF	working fluid

expectancies (up to 30 years), low costs if appropriately designed and operated, and small environmental footprints [3]. Unlike CAES that requires caverns to contain the compressed air and potential fossil-fuel combustion, LAES and PTES are free from geographical restrictions and have additional environmental benefits, making them promising for low-cost, large-scale and long-duration energy storage. The development of LAES technology is now approaching early commercialisation, while PTES alternatives are at a lower technology readiness level (TRL). Therefore, comprehensive studies on PTES are necessary to address the research and development gap.

In a conventional PTES system, electricity is converted into thermal energy by a heat pump cycle during charging, creating a temperature difference between two thermal stores; the stored thermal energy is later used to drive a power cycle and converted back into electricity during discharging [5]. According to the thermodynamic cycles employed, PTES is generally classified into three categories: (i) Joule-Brayton cycle-based PTES, (ii) Rankine cycle-based PTES, and (iii) transcritical cycle-based PTES, among which Joule-Brayton cycle-based PTES was the first to be proposed and studied [6]. At the same time, thermal energy storage (TES) technologies that are suitable and available for PTES consist of sensible heat, latent heat and thermochemical heat storage [2].

Packed-bed sensible-heat stores (PBSHSs) are a suitable store type due to their large heat transfer surfaces, small pressure losses, wide application ranges and low costs. PBSHSs undergo a transient heat transfer process so that unsteady packed-bed models (e.g., Schumann-type models [7]) need to be incorporated into PTES system models to clarify the thermodynamic losses. Desrues et al. [8] derived the global theoretical efficiency of PTES systems as a function of the ambient temperature, maximum system temperature, thermal compression ratio and polytropic efficiency, studied the transient energy storage/release performance of PTES systems with cycles by incorporating a Schumann-type thermal store model and obtained the system RTE at 67 %. White et al. [9–13] established modified Schumann-type thermal store models and discussed the effects of the operating temperature, reservoir geometry, operation mode, storage material, cycle duration and store configuration on the thermodynamic performance and pressure loss of packed-bed stores. Thermal loss coefficients were found to be 3.5–6.8 % for hot stores and 7.8–14 % for cold stores, respectively, under the typical operating conditions in the literature [9]. Later, White et al. [14] compared compression and expansion losses, pressure losses and thermal reservoir losses within whole PTES systems and investigated their impact on the system RTE, and McTigue et al. [15] further performed sensitivity analyses of the system RTE, energy density and power density to loss factors, operating conditions and geometric factors and conducted a multi-objective optimisation regarding the three thermodynamic performance factors. A RTE value of 70 % could be expected with reasonable estimates for mechanical and electrical losses. Following on from this work, Georgiou et al. [16,17] presented unified thermo-economic models of PTES and LAES systems, compared their technical and economic indicators, and assessed the thermo-economic performance when integrated into the whole electricity system in various scenarios.

In their work, Ni and Caram [18] adopted an exponential matrix solution to describe the thermal stores. They discussed the effects of the gas type, pressure ratio, dimensionless length and step time and turbomachinery polytropic efficiency on the system turn-around efficiency and storage utilisation ratio. However, this solution is not applicable to solve complicated engineering problems where parameters are dependent on temperature. Benato and Stoppato [19,20] selected the Mumma and Marvin model [21] for the heat transfer prediction in the thermal stores of a PTES configuration with an electrical heater used to raise the fluid temperature after compression, replacing the requirement for a high-temperature compressor. However, the RTE after adding an electrical heater was typically below 30 %, which motivated Chen et al. [22] to further consider integrating such PTES systems with organic Rankine cycle (ORC) power plants, which improved the RTE to 47 %. In the above studies, only the unsteadiness of thermal stores was considered, so Wang et al. [23] incorporated the unsteadiness of compressors, expanders and heat exchangers in PTES systems and analysed the influence of the pressure ratio, polytropic efficiency, particle diameter and reservoir structure on the system's performance. Wang et al. [24] also investigated the unbalanced flow rate in the packed-bed thermal stores caused by the differences in the temperatures and densities within the thermal front and found it had a limited effect on the system RTE.

As the operating pressure increases, especially in the heat store, a higher maximum temperature can be reached, leading to higher RTEs. However, a significant increase in the cost of the packed-bed stores will be associated as these are effectively pressure vessels. Liquid sensible-heat stores (LSHSs) consisting of a pair of non-pressurised vessels and a heat exchanger have been, therefore, proposed as possible alternatives. Laughlin [25] was the first researcher to propose Joule-Brayton cycle-based PTES with liquid sensible-heat stores. It was found that its RTE could be competitive with that of PHS and its cost could also be comparable to that of Joule-Brayton cycle-based PTES with PBSHSs. Farres-Antunez et al. [26] combined PTES and LAES using the same heat exchanger as the cold store, saving significant amounts of storage media per unit of stored energy. This new configuration delivered similar RTE values to those of separate systems, while having a significantly larger energy density. However, due to the limited working temperature ranges of common heat transfer fluids (HTFs), more than one set of LSHSs were needed to cover the full temperature range on the heat store side, which increased the complexity and cost of the system. This situation can be improved by incorporating recuperators. Zhao et al. [27] compared the exergy performance of recuperated and non-recuperated Joule-Brayton cycle-based PTES systems with liquid sensible-heat stores, and found that recuperators could lower the exergy destruction in the systems.

Although the above sensible-heat stores for Joule-Brayton cycle-based PTES systems are available off-the-shelf, efficient compressors and expanders operating at specific conditions (e.g., >500 °C or <−150 °C) with low thermodynamic losses are still immature and need further development, making experimental studies of PTES systems scarce. Howes [28] designed and tested a series of early-stage PTES system prototypes. The first grid-scale PTES demonstrator has been established at Newcastle University, which is rated at 150 kW and is capable of storing up to 600 kWh of electricity [29].

Sensible-heat stores have proven to be feasible options in Joule-Brayton cycle-based PTES systems, but their heat storage capabilities would limit the system energy density. Where this is an issue, the potential of deploying thermochemical-heat stores has been explored, as these are widely recognised to have the largest heat storage capacity among the available TES options [2]. Saghafifar et al. [30] proposed Joule-Brayton cycle-based PTES with packed-bed thermochemical-heat stores where a redox reaction is adopted to complete heat charging and discharging, and RTEs of 40–55 % at a capacity of 250–350 kWh/m^3 were reported. However, its operating temperature was limited to 900 K by the available compressor technology and only those solid oxides capable of releasing oxygen at low temperatures were feasible, which prevented the possible efficiency improvement. Saghafifar et al. [31] examined the storage media with higher decomposition temperatures and large reaction enthalpies, and added an electrical heater to increase the operating temperature. Similar RTEs and a higher capacity of 600–800 kWh/m^3 were achieved. Considering the technical complexity and unreadiness, Joule-Brayton cycle-based PTES with thermochemical-heat stores still remains at a conceptual stage.

Beyond sensible and thermochemical-heat stores, latent-heat stores are also considered as a promising option for Joule-Brayton cycle-based PTES applications thanks to their relatively high energy density and simple working principle [2]. Ge et al. [32] explored the thermodynamic feasibility of packed-bed latent-heat stores in PTES systems and evaluated the effects of the compression ratio, porosities, isentropic efficiencies, and inlet velocities on the systematic thermodynamic performance. The high operating pressure also increases the cost of packed-bed latent-heat stores as they are also effectively pressure vessels, and hence there is an opportunity to develop latent-heat stores whose cost is not sensitive to the operating pressure, such as shell-and-tube type latent-heat stores. Moreover, PTES systems have the potential to evolve from pure electricity storage operation to combined power, heating and cooling systems, because electricity is stored in the form of heat and cold. In order to make such combined power, heating and cooling systems satisfy the diverse energy demands of a wider energy system, heat and cold can be stored over a range of prescribed grades. Shell-and-tube cascaded latent-heat stores (CLHSs) have emerged as a promising option for deployment in Joule-Brayton cycle-based PTES systems, allowing these systems to produce power and multi-grade heat and cold at the same time with acceptable capital costs. In addition, due to the multi-grade heat and cold storage capability, it is also possible for a CLHS to recover external waste heat and/or cold sources at different grades, which further improves the RTE of the PTES system. However, although CLHSs offer the promise of such benefits in Joule-Brayton cycle-based PTES systems, the performance is not yet fully understood, which warrants the present investigation.

In this paper, a thermodynamic model of CLHSs based on exergy and entropy generation optimisation is developed and then used to explore the thermodynamic performance of CLHSs when these are deployed as heat stores in Joule-Brayton cycle-based PTES systems. The effects of the heat store arrangement (total stage number and stage area) and of the HTF velocity in the thermal store tubes on the heat storage and release rates of the whole store and of each stage, as well as the roundtrip efficiency, are evaluated. Two operation modes (pure electricity-storage mode and combined heating and power mode) are proposed to examine the potential of multi-energy supply. Finally, a comparison with PBSHSs and LSHSs is performed to assess the thermodynamic feasibility of CLHSs in Joule-Brayton cycle-based PTES systems.

2. Modelling methodology

2.1. Physical description

As illustrated in Fig. 1, in a shell-and-tube type CLHS, a total of N stages are deployed and each stage is filled with one kind of PCM. If $T_{m,i}$ is the PCM melting temperature of the i-th stage, and $T_{c,i}$ and $T_{d,N-i+1}$ are the HTF outlet temperatures of the i-th stage during charging and discharging, respectively, the PCMs are arranged in the decreasing order of melting temperatures along with the store length, namely $T_{m,1} > T_{m,2} > \ldots > T_{m,i-1} > T_{m,i} > T_{m,i+1} > \ldots > T_{m,N-1} > T_{m,N}$. During charging, the hot HTF (red colour in Fig. 1) flows in tubes along the direction of decreasing PCM melting temperatures and releases heat to multiple PCM stages, thus storing energy in the form of multi-grade latent heat; during discharging, the cold HTF (blue colour in Fig. 1) flows in the tubes in the opposite direction and absorbs heat from the PCMs, thus completing a cycle of operation. This is the operation mode that can provide thermal energy for electricity generation in PTES systems, and it is referred to in this work as a pure electricity-storage (PES) mode. The surplus heat in each stage can also be further utilised for various heating purposes so that power and multi-grade heat are supplied at the same time. This mode is referred to as a combined heating and power (CHP) mode.

A schematic diagram of a CLHS cross-section is given in Fig. 2, where D_s is the inner shell diameter, D_b is the bundle diameter, d_o and d_i are the outer and inner tube diameters, W is the width of each element, and d_{tp} is the tube pitch. The store can be divided into a number of cuboid elements, each of which contains one tube surrounded by PCMs. Several assumptions are made to simplify the physical problem:

(i) PCMs melt and solidify at a specific and constant (uniform and steady) temperature, T_m, not over a temperature range, and only latent heat is considered during the processes of thermal energy storage and release.
(ii) The thermophysical properties of the PCMs and of the HTF are constant, and the HTF temperature variation normal to the flow direction is negligible.
(iii) The heat transfer area of each stage, or stage area, A, is the same, and heat charging and discharging processes are of equal duration to simplify the balance between the energy supply and demand [9].
(iv) The melting temperature in each stage, $T_{m,i}$, is higher than or equal to the environmental temperature, T_e.
(v) The total HTF pressure loss is less than or equal to 10 % of the initial operating pressure, p_0.
(vi) The external insulation is enough such that heat losses to the environment are small enough to neglect.

In this study, argon is considered as the HTF. The HTF inlet and outlet temperatures during charging $T_{in,f,c}$ ($T_{c,0}$) and $T_{out,f,c}$ ($T_{c,N}$), HTF mass flow rate during charging and discharging $\dot{m}_f$, operating pressure p_0, and charging/discharging time τ have all been taken from a typical operational case in the literature [9]. The HTF inlet temperature during discharging $T_{in,f,d}$ ($T_{d,0}$) equals the environmental temperature T_e, which is 293 K. The above operating conditions are also kept fixed for PBSHSs and LSHSs to perform comparisons. The lowest temperature for direct heating in the CHP mode is 353 K [33]. The inner shell diameter D_s usually ranges from 0.06 m to 2 m [34]. Here, the upper bound is employed to make the whole store shorter and control the pressure loss. 3/4-in. O.D., 16 BWG (Birmingham Wire Gage) tubes are used whose d_o is 19 mm.

Over the investigated temperature range, organic and inorganic salt PCMs are usually used for heat storage, with densities mainly distributed over the range 800–2500 kg/m^3 and latent heats over the range 100–400 kJ/kg [2]. At the same time, although the thermal conductivity of organic and inorganic salts also varies over a wide range, it is relatively low, so that heat transfer enhancement is necessary. Michels and Pitz-Paal [35] suggested that the thermal conductivity of PCMs need to be at least 2 W/(m·K) to maintain fast and synchronous heat charging and discharging processes, and to make full use of CHLS technology. Given that this goal is easy to achieve through modern enhancement methods and multiple PCMs are adopted simultaneously, the thermal conductivities of the PCMs are all assumed to be 2 W/(m·K) in the present work [2]. Furthermore, considering that carbon steels can suffer from creep in high-pressure and long-term applications at temperatures above 700 K, the tubes and shells of the stores are made of stainless steel [25]. The operating conditions, geometrical parameters and thermophysical properties are summarised in Table 1 [9,34,36]. The average values of thermophysical properties under the operating condition are adopted.

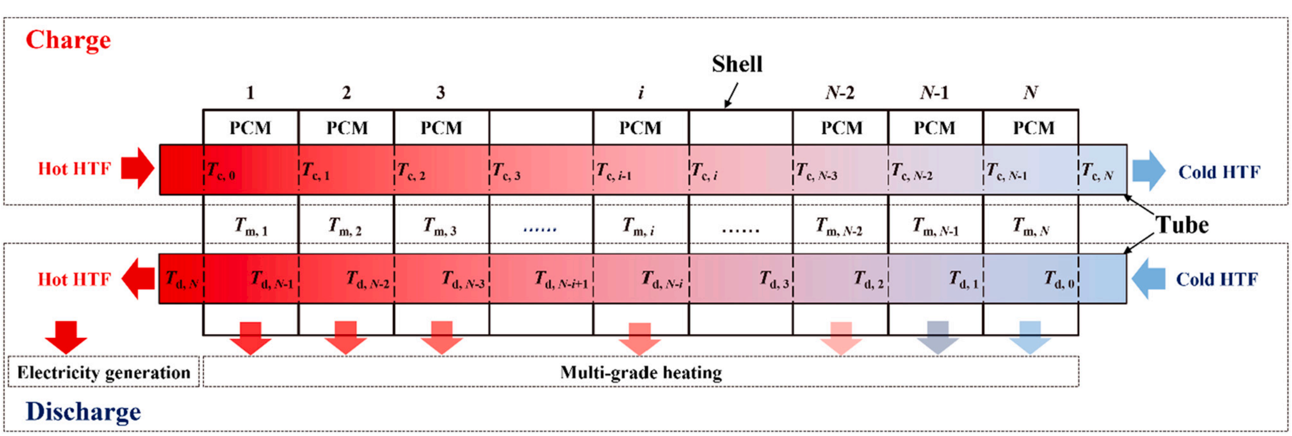

Fig. 1. Shell-and-tube type CLHS concept. (For interpretation of the references to colour in this figure, the reader is referred to the web version of this article.)

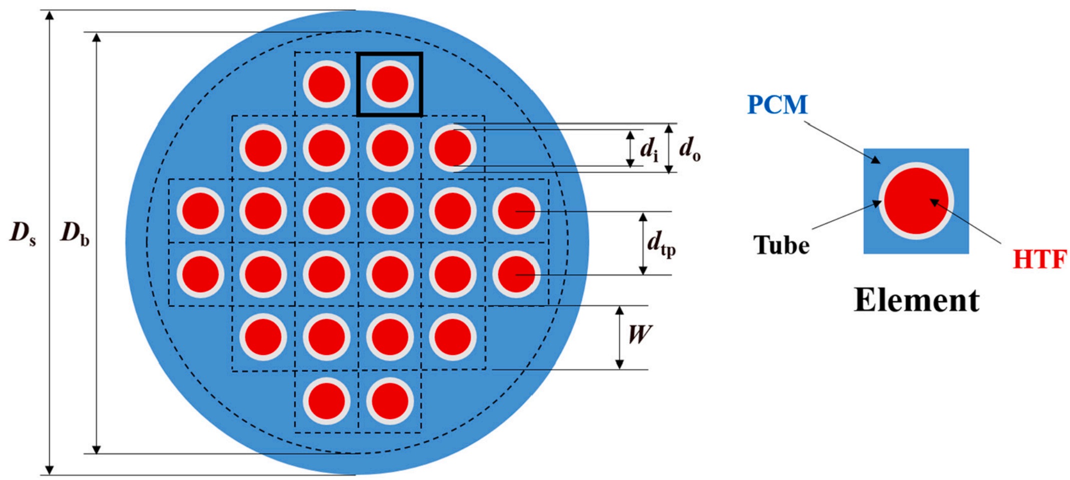

Fig. 2. Cross-section of shell-and-tube type CLHS.

Table 1
Operating conditions, geometrical parameters of CLHS and thermophysical properties of HTF and PCMs.

Operating conditions		
Argon inlet temperature during charging, $T_{in,f,c}$ ($T_{c,0}$)	K	773
Argon outlet temperature during charging, $T_{out,f,c}$ ($T_{c,N}$)	K	300
Argon inlet temperature during discharging, $T_{in,f,d}$ ($T_{d,0}$)	K	293
Operating pressure, p_0	bar	10
Environmental temperature, T_e	K	293
Argon mass flow rate, $\dot{m}_f$	kg/s	12.5
Charging/discharging time, τ	s	21600
Lowest temperature for direct heating, T_{heat}	K	353

Geometrical parameters		
Shell diameter, D_s	m	2
Tube outer diameter, d_o	m	1.9×10^{-2}
Tube inner diameter, d_i	m	1.57×10^{-2}

Thermophysical properties		
Specific heat capacity of argon, $c_{p,f}$	J/(kg·K)	524
Density of argon, ρ_f	kg/m^3	9.61
Thermal conductivity of argon, k_f	W/(m·K)	0.03
Prandtl number of argon, Pr_f	–	0.67
Dynamic viscosity of argon, μ_f	Pa·s	3.56×10^{-5}
Thermal conductivity of tube material, k_{tube}	W/(m·K)	21.4
Thermal conductivity of PCMs, k_{PCM}	W/(m·K)	2
Lower & upper limits of PCM density, $\rho_{PCM,1}$ & $\rho_{PCM,2}$	kg/m^3	800 & 2500
Lower & upper limits of PCM specific latent heat, $\Delta h_{PCM,1}$ & $\Delta h_{PCM,2}$	kJ/kg	100 & 400

2.2. Mathematical models

2.2.1. Charging process

During charging, the heat storage rate in the i-th stage is:

$$\dot{Q}_{st,c,i} = \dot{m}_f c_{p,f}\left(T_{c,i-1} - T_{c,i}\right) = U_i A_i \left\{\left(T_{c,i-1} - T_{c,i}\right) / ln\left[\left(T_{c,i-1} - T_{m,i}\right) / \left(T_{c,i} - T_{m,i}\right)\right]\right\} \tag{1}$$

where $\dot{m}_f$ is the argon mass flow rate, $c_{p,f}$ is the specific heat capacity of argon, $T_{c,i\text{-}1}$ and $T_{c,i}$ are the HTF inlet and outlet temperatures of the i-th stage, $T_{m,i}$ is the PCM melting temperature of the i-th stage, and U_i and A_i are the heat transfer coefficient and heat transfer area of the i-th stage.

The number of transfer units (NTU) in the i-th stage is:

$$\mathrm{NTU}_i = \left(U_i A_i\right) / \left(\dot{m}_f c_{p,f}\right) = ln\left[\left(T_{c,i-1} - T_{m,i}\right) / \left(T_{c,i} - T_{m,i}\right)\right] \tag{2}$$

Following Assumption (iii) in Section 2.1, and defining a parameter $C = e^{\mathrm{NTU}}$, then the melting temperature $T_{m,i}$ in the i-th stage can be described as:

$$T_{m,i} = \left(C T_{c,i} - T_{c,i-1}\right) / (C - 1) \tag{3}$$

The exergy storage rate in the i-th stage is:

$$\dot{E}x_{\mathrm{st,c},i} = \dot{Q}_{\mathrm{st,c},i}\left(1 - T_{\mathrm{e}}/T_{\mathrm{m},i}\right) \tag{4}$$

where T_{e} is the environmental temperature, such that the total exergy storage rate in the whole store is then:

$$\dot{E}x_{\mathrm{st,c,tot}} = \sum_{i=1}^{N}\dot{E}x_{\mathrm{st,c},i} = \sum_{i=1}^{N}\left[\dot{Q}_{\mathrm{st,c},i}\left(1 - T_{\mathrm{e}}/T_{\mathrm{m},i}\right)\right] \tag{5}$$

where N is the total stage number.

Moreover, the entropy generation rate in the i-th stage is:

$$\dot{S}_{\mathrm{g,c},i} = \Delta\dot{S}_{\mathrm{c},i} - \dot{S}_{\mathrm{f,c},i} - \dot{m}_{\mathrm{f}}\left(s_{\mathrm{c},i-1} - s_{\mathrm{c},i}\right) = \dot{m}_{\mathrm{f}}c_{\mathrm{p,f}}\left[ln\left(T_{\mathrm{c},i}/T_{\mathrm{c},i-1}\right) + \left(T_{\mathrm{c},i-1} - T_{\mathrm{c},i}\right)/T_{\mathrm{m},i}\right] \tag{6}$$

where $\Delta\dot{S}_{\mathrm{c},i}$ and $\dot{S}_{\mathrm{f,c},i}$ are the entropy change rate and entropy flow rate in the i-th stage, and $s_{\mathrm{c},i\text{-}1}$ and $s_{\mathrm{c},i}$ are the specific entropy at the inlet and outlet of the i-th stage.

The total entropy generation rate in the whole store is then obtained from:

$$\dot{S}_{\mathrm{g,c,tot}} = \sum_{i=1}^{N}\dot{S}_{\mathrm{g,c},i} = \dot{m}_{\mathrm{f}}c_{\mathrm{p,f}}\sum_{i=1}^{N}\left[ln\left(T_{\mathrm{c},i}/T_{\mathrm{c},i-1}\right) + \left(T_{\mathrm{c},i-1} - T_{\mathrm{c},i}\right)/T_{\mathrm{m},i}\right] \tag{7}$$

2.2.2. Discharging process

During discharging, the melting temperature in each stage $T_{\mathrm{m},i}$ is the same as that of the charging process. In the i-th stage, the ideal outlet temperature is defined as the upper limit that can be achieved:

$$T_{\mathrm{d},N-i+1}^{\mathrm{ideal}} = \frac{C-1}{C}T_{\mathrm{m},i} + \frac{1}{C}T_{\mathrm{d},N-i} \tag{8}$$

Then the ideal heat release rate in the i-th stage is:

$$\dot{Q}_{\mathrm{re,d},i}^{\mathrm{ideal}} = \dot{m}_{\mathrm{f}}c_{\mathrm{p,f}}\left(T_{\mathrm{d},N-i+1}^{\mathrm{ideal}} - T_{\mathrm{d},N-i}\right) \tag{9}$$

$$\frac{\partial\dot{E}x_{\mathrm{st,c,tot}}}{\partial T_{\mathrm{c},i}} = \begin{cases} \dot{m}_{\mathrm{f}}c_{\mathrm{p,f}}T_{\mathrm{e}}(C-1)^2\left[T_{\mathrm{c},i-1}\Big/\left(CT_{\mathrm{c},i} - T_{\mathrm{c},i-1}\right)^2 - T_{\mathrm{c},i+1}\Big/\left(CT_{\mathrm{c},i+1} - T_{\mathrm{c},i}\right)^2\right] = 0, & 1 \le i \le N-1 \\ \dot{m}_{\mathrm{f}}c_{\mathrm{p,f}}\left[(C-1)^2T_{\mathrm{e}}T_{\mathrm{c},i-1}\Big/\left(CT_{\mathrm{c},i} - T_{\mathrm{c},i-1}\right)^2 - 1\right] = 0, & i = N \end{cases} \tag{16}$$

According to Assumption (iii) in Section 2.1, heat charging and discharging processes are of equal duration, so the heat storage rate $Q_{\mathrm{st,c},i}$ in each stage is larger than or equal to the heat release rate in each stage $Q_{\mathrm{re,d},i}$ and the outlet temperature in the i-th stage is finally expressed as:

$$T_{\mathrm{d},N-i+1} = \begin{cases} \dfrac{C-1}{C}T_{\mathrm{m},i} + \dfrac{1}{C}T_{\mathrm{d},N-i}, & \dot{Q}_{\mathrm{re,d},i}^{\mathrm{ideal}} \le \dot{Q}_{\mathrm{st,c},i} \\ T_{\mathrm{c},i-1} - T_{\mathrm{c},i} + T_{\mathrm{d},N-i}, & \dot{Q}_{\mathrm{re,d},i}^{\mathrm{ideal}} > \dot{Q}_{\mathrm{st,c},i} \end{cases} \tag{10}$$

where $T_{\mathrm{d},N\text{-}i}$ is the i-th stage argon inlet temperature.

The heat release rate in the PES mode in the i-th stage is thus:

$$\dot{Q}_{\mathrm{re,d},i,\mathrm{PES}} = \dot{m}_{\mathrm{f}}c_{\mathrm{p,f}}\left(T_{\mathrm{d},N-i+1} - T_{\mathrm{d},N-i}\right) \tag{11}$$

and the heat release rate for direct heating in the i-th stage is:

$$\dot{Q}_{\mathrm{re,d},i,\mathrm{heat}} = \begin{cases} \dot{Q}_{\mathrm{st,c},i} - \dot{Q}_{\mathrm{re,d},i,\mathrm{PES}}, & T_{\mathrm{m},i} \ge 353\mathrm{K} \\ 0, & T_{\mathrm{m},i} < 353\mathrm{K} \end{cases} \tag{12}$$

The heat release rate in the CHP mode in the i-th stage is:

$$\dot{Q}_{\mathrm{re,d},i,\mathrm{CHP}} = \dot{Q}_{\mathrm{re,d},i,\mathrm{PES}} + \dot{Q}_{\mathrm{re,d},i,\mathrm{heat}} \tag{13}$$

Finally, the total heat release rates in the PES and CHP modes in the whole store are:

$$\dot{Q}_{\mathrm{re,d,tot,PES}} = \sum_{i=1}^{N}\dot{Q}_{\mathrm{re,d},i,\mathrm{PES}};\ \dot{Q}_{\mathrm{re,d,tot,CHP}} = \sum_{i=1}^{N}\dot{Q}_{\mathrm{re,d},i,\mathrm{CHP}} \tag{14}$$

For the CLHS, the roundtrip efficiency (RTE) is defined as the thermal energy output divided by the thermal energy input to the store as follows:

$$\mathrm{RTE} = \frac{Q_{\mathrm{re,d,tot}}}{Q_{\mathrm{st,c,tot}}} = \frac{\int_0^{\tau}\dot{Q}_{\mathrm{re,d,tot}}dt}{\int_0^{\tau}\dot{Q}_{\mathrm{st,c,tot}}dt} \tag{15}$$

2.2.3. Determination of melting temperatures

For a given HTF temperature profile within the CLHS, the distribution of the melting temperatures of the various stages affects the HTF outlet temperatures, heat transfer rates and exergy losses of each stage, and also of the whole store directly. To increase the flexibility of the CLHS in energy allocation for power generation and heating when operating PTES systems in CHP mode, the lowest thermodynamic loss during charging is expected and therefore two optimisation methods originating from the second law of thermodynamics are used to obtain the optimal distribution of melting temperatures: (i) maximisation of the total exergy storage rate, and (ii) minimisation of the total entropy generation rate.

When maximising the total exergy storage rate, the following expressions should be satisfied:

$$\frac{\partial^2\dot{E}x_{\mathrm{st,c,tot}}}{\partial T_{\mathrm{c},i}{}^2} < 0 \tag{17}$$

The Lagrange multiplier method is used to minimise the total entropy generation rate subjected to the constraint that the total heat storage rate is constant. A Lagrangian function is defined as follows:

$$G\left(T_{\mathrm{c},1}, T_{\mathrm{c},2}, \cdots T_{\mathrm{c},i}\cdots, T_{\mathrm{c},N-1}, T_{\mathrm{c},N}, \delta\right) = \dot{S}_{\mathrm{g,c,tot}} + \delta\left(\dot{Q}_{\mathrm{st,c,tot}} - \theta\right) \tag{18}$$

where δ is the Lagrange multiplier and θ is the constant heat storage rate during charging.

The following expressions should be satisfied:

$$\frac{\partial G}{\partial T_{c,i}} = \begin{cases} \dot{m}_f c_{p,f}(C-1)^2\left[-T_{c,i-1}\Big/\left(CT_{c,i}-T_{c,i-1}\right)^2 + T_{c,i+1}\Big/\left(CT_{c,i+1}-T_{c,i}\right)^2\right] = 0, & 1 \le i \le N-1 \\ \dot{m}_f c_{p,f}\left[1\Big/T_{c,i} - (C-1)^2 T_{c,i-1}\Big/\left(CT_{c,i}-T_{c,i-1}\right)^2 - \delta\right] = 0, & i = N \end{cases} \tag{19}$$

$$\frac{\partial G}{\partial \delta} = \dot{m}_f c_{p,f}\left(T_{c,0} - T_{c,N}\right) - \theta = 0 \tag{20}$$

$$\frac{\partial^2 G}{\partial {T_{c,i}}^2} > 0 \tag{21}$$

$$\frac{\partial^2 G}{\partial \delta^2} > 0 \tag{22}$$

It is found that there exists the same analytical solution to the outlet temperature of the i-th stage during charging, $T_{c,i}$, for the above two optimisation problems by solving Eqs. (16) and (17), and Eqs. (19), (20), (21) and (22):

$$T_{c,i,opt} = T_{c,0}\left(T_{c,N}/T_{c,0}\right)^{i/N} \tag{23}$$

The analytical solution to the melting temperature in the i-th stage is then obtained by substituting Eq. (23) into Eq. (3) and is given by the expression:

$$T_{m,i,opt} = \left(CT_{c,i,opt} - T_{c,i-1,opt}\right)\Big/(C-1) = T_{c,0}\left(T_{c,N}/T_{c,0}\right)^{(i-1)/N}\left[C\left(T_{c,N}/T_{c,0}\right)^{1/N} - 1\right]\Big/(C-1) \tag{24}$$

2.2.4. Determination of design parameters

In the CLHS, the inner shell diameter D_s and the bundle diameter D_b satisfy [34]:

$$D_b = 9.995D_s - 0.012 - d_o \tag{25}$$

where d_o is the outer tube diameter, while the tube pitch d_{tp} can be estimated from [34]:

$$d_{tp} = \sqrt{\frac{0.78}{n_{tube}}}D_b \tag{26}$$

and the tube number n_{tube} in each stage is:

$$n_{tube} = \left[\frac{4\dot{m}_f}{\pi\rho_f v_{tube} d_i^2}\right] \tag{27}$$

where $\dot{m}_f$ is the total HTF mass flow rate, ρ_f is the HTF density, v_{tube} is the HTF velocity in the tubes of the heat store, or tube-side velocity, and d_i is the inner tube diameter.

The length of each stage L is determined by the stage area A, and restricted by the PCM volume and pressure loss:

$$L = \frac{A}{n_{tube}\pi d_o} \tag{28}$$

Considering that multiple PCMs are deployed with wide ranges of specific latent heat and density, the length of each stage L should satisfy the following correlation to make sure the space inside the store matches PCM volume:

$$\frac{\int_0^\tau \dot{Q}_{st,c,i}dt}{\Delta h_{PCM,1}\rho_{PCM,1}\left(\pi D_s^2/4 - \pi d_o^2 n_{tube}/4\right)} \le L \le \frac{\int_0^\tau \dot{Q}_{st,c,i}dt}{\Delta h_{PCM,2}\rho_{PCM,2}\left(\pi D_s^2/4 - \pi d_o^2 n_{tube}/4\right)} \tag{29}$$

where $Q_{st,c,i}$ is the heat storage rate in the i-th stage, τ is the charging time, $\Delta h_{PCM,1}$ and $\Delta h_{PCM,2}$ are the upper and lower limits of PCM specific latent heat, and $\rho_{PCM,1}$ and $\rho_{PCM,2}$ are the upper and lower limits of PCM density.

Additionally, the length of each stage L should also satisfy the following relation to meet the pressure loss requirement:

$$L \le \frac{2d_i\Delta p}{f\rho_f v_{tube}^2 N} \tag{30}$$

where Δp is the pressure loss and less than or equal to 10 % p_0, and f is the friction factor determined from [37]:

$$f = \frac{1}{(0.79lnRe - 1.64)^2} = \frac{1}{\left(0.79ln\frac{\rho_f v_{tube} d_i}{\mu_f} - 1.64\right)^2} \tag{31}$$

where Re is the Reynolds number, ρ_f is the HTF density, v_{tube} is the HTF tube-side velocity, d_i is the inner tube diameter, and μ_f is the HTF dynamic viscosity.

The length of each stage L is finally determined through Eqs. (28), (29) and (30).

As shown in Fig. 2, each element is the same, making the heat transfer coefficient U in each element equal to each other and expressed as [38]:

$$U = \frac{1}{d_o/(h_i d_i) + d_o ln(d_o/d_i)/(2k_{tube}) + d_o ln(1.08W/d_o)/(2k_{PCM})} \tag{32}$$

where k_{tube} and k_{PCM} are the thermal conductivities of the tube and PCMs, and h_i is the inner convective heat transfer coefficient inside tubes.

The lowest HTF tube-side velocity v_{tube} is obtained using Eqs. (25), (26) and (27) when the tube pitch d_{tp} equals the outer tube diameter d_o, so that the maximum number of tubes can be deployed at a fixed HTF total flow rate. In this case, the lowest HTF tube-side velocity v_{tube} is calculated to be 0.8 m/s, corresponding to a Reynolds number of 3430, so that the flow remains turbulent. In addition, the velocity should be below 60 to 80 ft/s (i.e., 17–22 m/s) to minimise noise and allow for corrosion inhibition [39]. In this study, the highest HTF tube-side

Table 2
Comparison between predictions from the present study and the results reported in Ref. [40].

	HTF outlet temperature		Melting temperature	
	Present study	Ref. [40]	Present study	Ref. [40]
Stage 1	850	850	783	783
Stage 2	723	723	666	666
Stage 3	614	614	566	566
Stage 4	522	522	481	481
Stage 5	444	444	409	409
Stage 6	377	377	348	348

velocity v_{tube} is set to 20 m/s, leading to a Reynolds number of 85000.

Considering operation of the store such that $0.5 < Pr_f < 2000$ and $3000 < Re < 5 \times 10^{20}$, the inner convective heat transfer coefficient h_i satisfies Gnielinski's correlation [37]:

$$h_i = \frac{k_f}{d_i} Nu = \frac{k_f}{d_i} \frac{(f/8)(Re - 1000)Pr_f}{1 + 12.7(f/8)^{1/2}\left(Pr_f^{2/3} - 1\right)} \tag{33}$$

where Nu is the Nusselt number, k_f is the HTF thermal conductivity, d_i is the inner tube diameter, f is the friction factor, Re is the Reynolds number, and Pr_f is the Prandtl number.

2.3. Numerical methodology

2.3.1. Model verification

Models of the aforementioned CLHSs were developed in MATLAB, and then verified by comparing their predictions with results taken from Ref. [40], specifically considering the HTF outlet temperature and melting temperature of each stage. The HTF inlet and outlet temperatures of the whole store during charging are 1000 K and 377 K with a total of six stages deployed. Table 2 compares the results of the present study to those in Ref. [40]. It is found that the HTF outlet temperature and melting temperature of each stage in the present study are equal to those of each stage in Ref. [40], because the HTF outlet temperature and melting temperature of each stage in these two studies are calculated from the analytical solutions: Eqs. (23) and (24).

2.3.2. Calculation procedure

From the CLHS model described in Section 2.2, it is found that the total stage number N and NTU in each stage are two key parameters that affect the outlet and melting temperature distributions as well as the heat storage and release rates of each stage and of the whole store. The NTU, as defined in Eq. (2), is a dimensionless parameter that is widely used for heat exchanger analysis and expands to the design of shell-and-tube type heat stores, however, it is still not a direct parameter to guide the corresponding design work. From Eq. (2), it can be seen that the NTU is a function of the heat transfer coefficient U and stage area A, while Eqs. (31), (32) and (33) indicate that the heat transfer coefficient U itself is a function of the HTF tube-side velocity v_{tube} and the stage area A. Therefore, the NTU is expressed in terms of the HTF tube-side velocity v_{tube} and stage area A. The total stage number N and stage area A are regarded as parameters that characterise the design of the heat store arrangement, and the HTF tube-side velocity v_{tube} is a parameter related to the stores' operation.

In the calculation procedure, the analytical solution to melting temperatures is first obtained by maximisation of the total exergy storage rate and minimisation of the total entropy generation rate. Combined with the operating conditions, geometry parameters and thermophysical properties, some key parameters, including NTU, melting temperature, outlet temperature (charging, stage and store), heat storage rate (stage and store), tube number, stage length and friction factor, are calculated using the design and operating variables (N, A and v_{tube}). Then, regarding the constrains in terms of the melting temperature, PCM volume and pressure loss, the valid region of total stage number N and stage area A corresponding to a specific HTF tube-side velocity v_{tube} is determined. Also, the ideal outlet temperature (discharging, stage) and heat release rate (stage) are obtained. Finally, based on the energy balance between charging and discharging, the heat release rates (stage and store) during discharging as well as the RTE are acquired. The calculation procedure is performed using MATLAB and shown in Fig. 3.

3. Results and discussion

In this section, the effects of total stage number N, stage area A and HTF tube-side velocity v_{tube} on the outlet and melting temperature distributions, the heat storage and release rates of both each individual stage and of the whole store, as well as the RTE of the store are discussed. The total heat storage rate of the CLHS is set to 3.10 MW in all cases, by imposing the HTF mass flow rate, specific heat capacity, and inlet and outlet temperatures summarised in Table 1. The total stage number N ranges from 1 to 100, with each stage regarded as a heat exchanger with stage area A ranging from 10 m^2 to 1000 m^2 [41].

3.1. Heat store arrangement

3.1.1. Charging process

(1) Total heat storage rate

According to the CLHS model described in Sections 2.1 and 2.2, the total heat storage rate of the whole store is constant (set to 3.10 MW) and is not affected by the total stage number N and stage area A. However, not all the stage numbers N and stage areas A within the investigated ranges are feasible, which leads to a region of valid designs with total stage numbers N and stage areas A allowed by Assumption (iv) in Section 2.1 and the restrictions of the PCM volume and HTF pressure loss in Eqs. (29) and (30). Assumption (iv) can provide a preliminary valid region of total stage number N and stage area A from the perspective of temperature distributions. Eqs. (29) and (30) restrict the valid region of total stage number N and stage area A with respect to the PCM volume and HTF pressure loss, which are actually determined by the HTF tube-side velocity v_{tube}. In other words, outside the valid design region, it is not possible to ensure that the melting temperature in each stage is higher than the environmental temperature, the volume of each stage is compatible with the appropriate PCM, and the HTF pressure loss is less than or equal to 0.1 MPa at the same time.

In Fig. 4, the valid regions of total stage number N and stage area A are illustrated for HTF tube-side velocities v_{tube} = 0.8 m/s, 5 m/s, 10 m/s, 15 m/s and 20 m/s, respectively. It is found that lower HTF tube-side velocities v_{tube} lead to a larger number of tubes and smaller cross sections for PCMs in each stage, and therefore, a longer stage length L and more stages required to contain the total PCM volume, leading to larger total stage numbers and areas. Thus, when the HTF tube-side velocity is at the lowest value within the investigated range, v_{tube} = 0.8 m/s, the valid region of N and A corresponds to the largest total stage numbers and stage areas, which is mainly determined by the PCM volume restriction. When the HTF tube-side velocity v_{tube} increases to 5 m/s, the valid region of total stage number N and stage area A is formed by the restrictions to both the PCM melting temperature and volume. The increase in the HTF tube-side velocity v_{tube} is associated with a decrease in the tube number and an increase in the cross section, which means a smaller total stage numbers and stage areas in order to provide enough space for the PCMs. As the HTF tube-side velocity v_{tube} increases further, the restriction imposed on the pressure loss also begins to play an increasingly important role. When the HTF tube-side velocity v_{tube} is 10 m/s or 15 m/s, the valid region is dominated by combined restrictions to the PCM melting temperature, volume and the HTF pressure loss, making the valid region of N and A narrower with decreasing the total

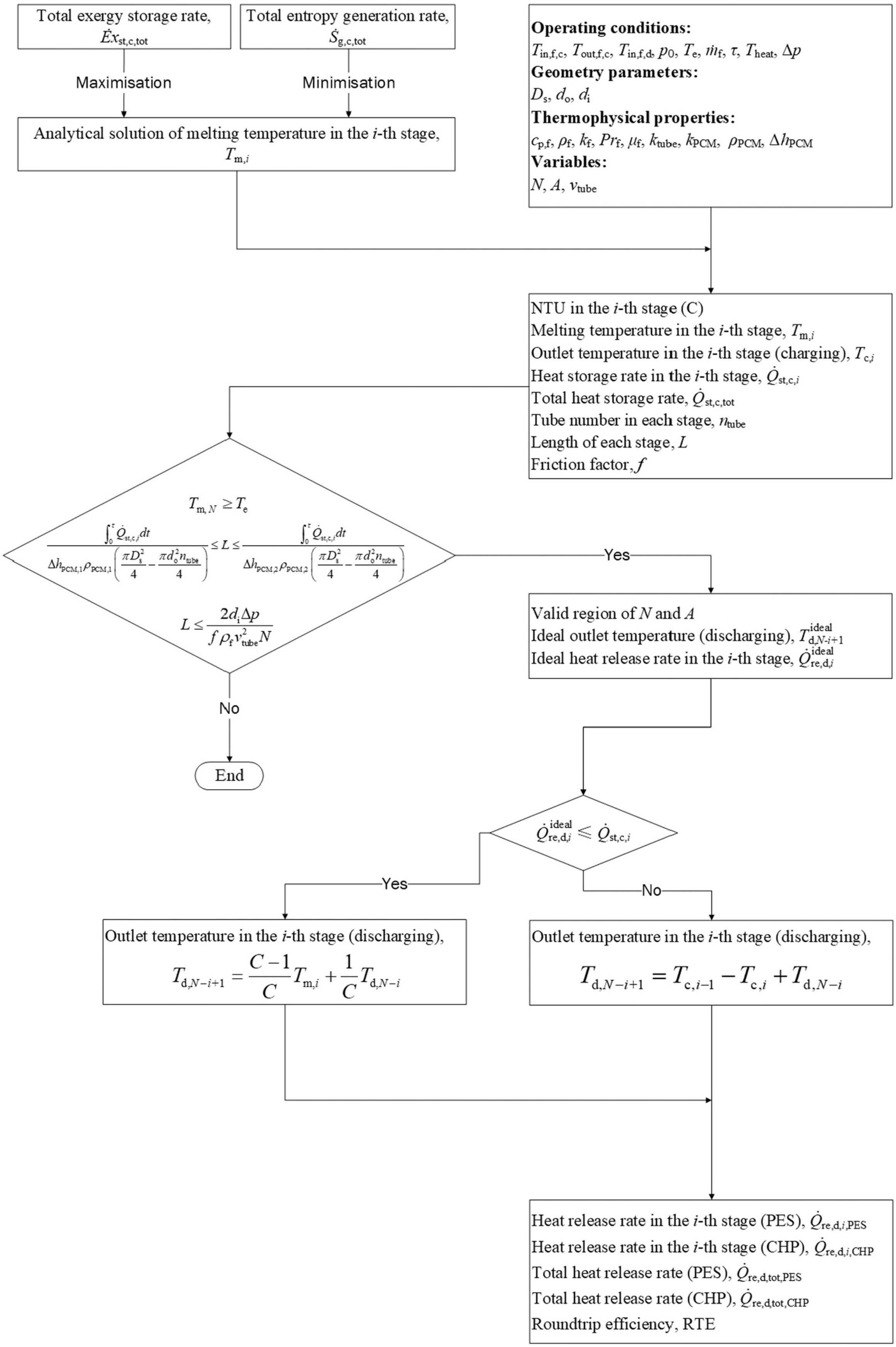

Fig. 3. Flowchart of model solution as implemented in MATLAB.

stage number N and stage area A. At the highest HTF tube-side velocity, $v_{tube} = 20$ m/s, the valid region of total stage number N and stage area A reduces to a much smaller region, approaching a line.

(2) Temperature and heat storage rate distributions

According to Eqs. (23) and (24), the PCM melting temperature and HTF outlet temperature in each stage should be arranged in a decreasing geometric progression along the HTF flow direction. Then, the heat storage rate in each stage can be obtained by Eq. (1). In Fig. 5, the temperature and heat storage rate distributions in each stage during charging are given when the total stage numbers N are 10, 15 and 20, respectively. The stage area A is 300 m^2 and the HTF tube-side velocity v_{tube} is 5 m/s.

In Fig. 5(a), the PCM melting temperature $T_{m,i}$, HTF outlet temperature $T_{c,i}$ in each stage and their difference decreases along the HTF flow direction. The melting temperature ranges are 298–698 K, 298–722 K and 299–734 K, when the total stage numbers N are 10, 15 and 20, meaning that the melting temperature distribution can be widened significantly by increasing the total stage number N while also storing thermal energy in more energy grades. Furthermore, the temperature difference between the HTF and PCM in each stage also decreases with the total stage number N. Specifically, the average logarithmic mean temperature differences (LMTDs) over the stages are found to be 18 K, 12 K and 9 K, respectively, when the total stage numbers N are 10, 15 and 20, which indicates that the thermodynamic loss caused by irreversible heat transfer can be avoided by increasing the total stage number N. In Fig. 5(b), the heat storage rate in each stage is found to decrease along the HTF flow direction, showing that the inlet stages play a more important role in the heat storage process. It is also found that the heat storage rate in each stage can be adjusted to be distributed more uniformly by increasing the total stage number N. When the total stage numbers N are 10, 15 and 20, the ranges of the heat storage rate in each stage are 195–458 kW, 128–310 kW and 95–234 kW, respectively.

Fig. 6 considers the role of the stage area, by showing the temperature and heat storage rate distributions in each stage when the stage areas A are 200 m^2, 300 m^2 and 400 m^2. The total stage number N is 15 and the HTF tube-side velocity v_{tube} is 5 m/s. In Fig. 6(a), the PCM melting temperature $T_{m,i}$, HTF outlet temperature $T_{c,i}$ and temperature difference in each stage show similar decreasing trends along the HTF

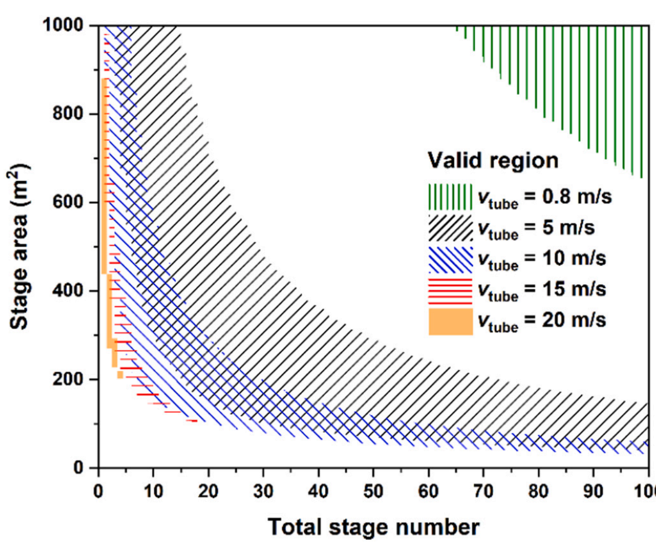

Fig. 4. Valid region for CLHS design in terms of total stage number N and stage area A with different HTF tube-side velocities v_{tube}. Green line domain: v_{tube} = 0.8 m/s, black line domain: v_{tube} = 5 m/s, blue line domain: v_{tube} = 10 m/s, red line domain: v_{tube} = 15 m/s, and orange domain: v_{tube} = 20 m/s. (For interpretation of the references to colour in this figure legend, the reader is referred to the web version of this article.)

flow direction to those in Fig. 5(a). For different stage areas, the HTF outlet temperatures in each stage are the same, while a larger stage area leads to a wider distribution of melting temperatures. The ranges of melting temperatures are 296–716 K, 298–722 K and 299–724 K, respectively, when the stage areas A are 200 m^2, 300 m^2 and 400 m^2. Further, as the stage area A increases, the melting temperatures in each stage approach the corresponding outlet temperatures, reducing the temperature differences in each stage. The average LMTDs over the stages are 18 K, 12 K and 9 K, when the stage areas A are 200 m^2, 300 m^2 and 400 m^2, respectively.

Fig. 6(b) turns to the heat storage rate in the CLHS. It is found that the heat storage rate in each stage decreases along the HTF flow direction, confirming the vital role of inlet stages in the heat storage process. For different stage areas, the distribution of heat storage rates in each stage remains the same.

3.1.2. Discharging process

(1) Total heat release rate and roundtrip efficiency

Since the total heat storage rate is constant at 3.10 MW and the charging and discharging times are both 6 h, the RTE follows a similar trend the total heat release rate. As with the total heat storage rate, the valid region of total stage number N and stage area A for the total heat release rate and RTE is strongly affected by the HTF tube-side velocity v_{tube}. In the CLHS model description in Section 2.1, it was mentioned that the discharging process can be aimed at pure-electricity storage (PES) operation or combined heating and power (CHP) operation, and it is expected that the total heat release rates and RTEs of the two modes will be different.

Fig. 7 shows the variation of the total heat release rate and of the RTE in the PES mode with respect to the total stage number N and stage area A. Four HTF tube-side velocities, i.e., v_{tube} = 0.8 m/s, 5 m/s, 10 m/s and 15 m/s, are selected. In Fig. 7(a), the total heat release rate of the store varies in a small range from 3.06 MW to 3.09 MW and is close to the total heat storage rate of 3.10 MW with the RTE ranging over a narrow range from 98.7 % to 99.7 % when the HTF tube-side velocity v_{tube} reaches its minimum value of 0.8 m/s. The corresponding pairs of total stage number N and stage area A for the maxima and minima are (100, 1000 m^2) and (65, 990 m^2), respectively. As the HTF tube-side velocity v_{tube} increases to 5 m/s, the valid region of total stage number N and stage area A expands as shown in Fig. 7(b). It is found that the total heat release rate is lower than 2.00 MW when the total stage number N is less than or equal to 3 and reaches the minimum at 1.77 MW with the RTE being 57.2 % when the total stage number N is 3 and stage area A is 860 m^2. The maxima of the total heat release rate and RTE remain at 3.06 MW and 98.7 %, which is obtained when the total stage number N is 100 and stage area A is 150 m^2. It is also shown that an RTE value above 85 % can be achieved at most of the pairs of total stage number N and stage area A within the investigated region. In Fig. 7(c), the HTF tube-side velocity v_{tube} is increased further to 10 m/s, for which fewer pairs of total stage number N and stage area A can achieve RTE values above 85 %. The highest total heat release rate and RTE (achieved when the total stage number N is 100 and stage area A is 60 m^2), drops to 3.00 MW and 96.7 %, respectively. The single-stage store (N = 1) can satisfy the restrictions of PCM melting temperature, volume and HTF pressure loss, but it has the very low RTE of 1.4 %. When the HTF tube-side velocity v_{tube} is 15 m/s, as shown in Fig. 7(d), the highest total heat release rate and RTE are 2.72 MW and 87.8 %, which are achieved when the total stage number N is 22 and stage area A is 90 m^2, respectively. The RTE of most pairs of total stage number N and stage area A is below 85 % and the lowest RTE is also 1.4 %, when a single-stage store is deployed. In summary, the pair of the total stage number N and stage area A to achieve the optimal thermodynamic performance varies with the HTF tube-side velocity and the single-stage store is not feasible in the PTES system.

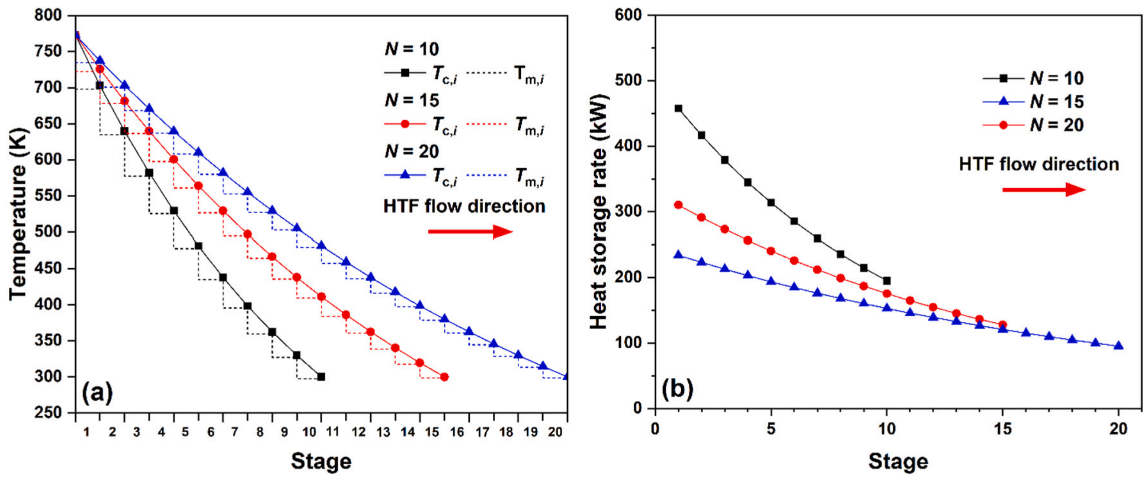

Fig. 5. Characteristics of each stage in CLHS during charging: (a) PCM melting and HTF outlet temperatures, and (b) heat storage rate. Stage area A is 300 m^2, HTF tube-side velocity v_{tube} is 5 m/s and total stage numbers N = 10, 15 and 20 are considered.

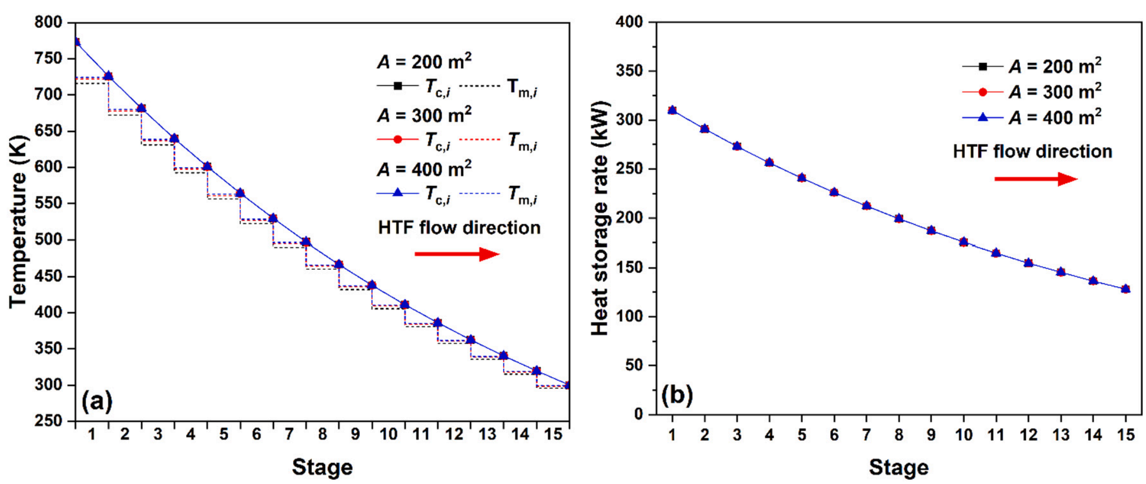

Fig. 6. Characteristics of each stage in CLHS during charging: (a) PCM melting and HTF outlet temperatures, and (b) heat storage rate. Total stage number N is 15, HTF tube-side velocity v_{tube} is 5 m/s and stage areas A = 200 m^2, 300 m^2 and 400 m^2 are considered.

The total heat release rate and RTE in the CHP mode are shown as a function of the total stage number N and stage area A in Fig. 8 for four HTF tube-side velocities v_{tube} = 0.8 m/s, 5 m/s, 10 m/s and 15 m/s. In Fig. 8(a), when the HTF tube-side velocity v_{tube} is 0.8 m/s, the total heat release rate of the store is higher than that in the PES mode (shown in Fig. 7) and attains the maximum value of 3.10 MW with the RTE being 100 % within the valid region of total stage number N and stage area A, which means that all the stored thermal energy can be used in CHP mode by the utilisation of surplus thermal energy for multi-grade heating. In Fig. 8(b), when the HTF tube-side velocity v_{tube} increases to 5 m/s in the CHP mode, unlike the PES mode, the total heat release rate is found to be higher than 2.00 MW across the whole valid region, and the RTE is higher than or equal to 85 % if the total stage number N is great than or equal to four. The minima of the total heat release rate and RTE are 2.42 MW and 77.9 %, which are obtained when the pair of total stage number N and stage area A is (3, 860 m^2). The maxima are still 3.10 MW and 100 %, which can be achieved within a specific narrow region of total stage number N and stage area A as shown in Fig. 8(b). In Fig. 8(c) and 8(d), when the HTF tube-side velocity v_{tube} is 10 m/s or 15 m/s, the valid region of total stage number N and stage area A further shrinks, and the single-stage store (N = 1) is feasible. However, the lowest total heat release rate and RTE are 0.04 MW and 1.4 %, which are as low as those in the PES mode, because the melting temperature in the single-stage store is below 353 K and the stored heat cannot be used for heating. When the HTF tube-side velocity v_{tube} is 10 m/s, the maxima of the total heat release rate and RTE are 3.08 MW and 99.3 % when the total stage number N is 97 and stage area A is 60 m^2. The maxima of the total heat release rate and RTE are 2.94 MW and 94.9 % when the HTF tube-side velocity is 15 m/s, which is obtained when the total stage number N is 20 and stage area A is 100 m^2.

Fig. 9 shows the total heat release rates for electricity generation, heating and both in CHP mode as a function of the total stage number N and stage area A. In Fig. 9(a), for the investigated stage areas A (200 m^2, 300 m^2 and 400 m^2), the total heat release rate for electricity generation increases with the total stage number N, while the total heat release rate for heating purposes decreases. The total heat release rate in the CHP mode, which is the sum of the total heat release rates for electricity generation and heating, increases and approaches 3.10 MW as an upper bound. The critical total stage numbers to reach the steady total heat release rate for the CHP mode are 57, 47 and 36, for the stage areas of 200 m^2, 300 m^2 and 400 m^2. In Fig. 9(b), three total stage numbers, 10, 15 and 20, are selected. For these three total stage numbers, a larger stage area leads to higher total heat release rates in both the PES (electricity generation) and CHP modes, and a lower total heat release rate for heating. It is also found that the corresponding total heat release rates tend to be constant when the stage area A increases to a certain

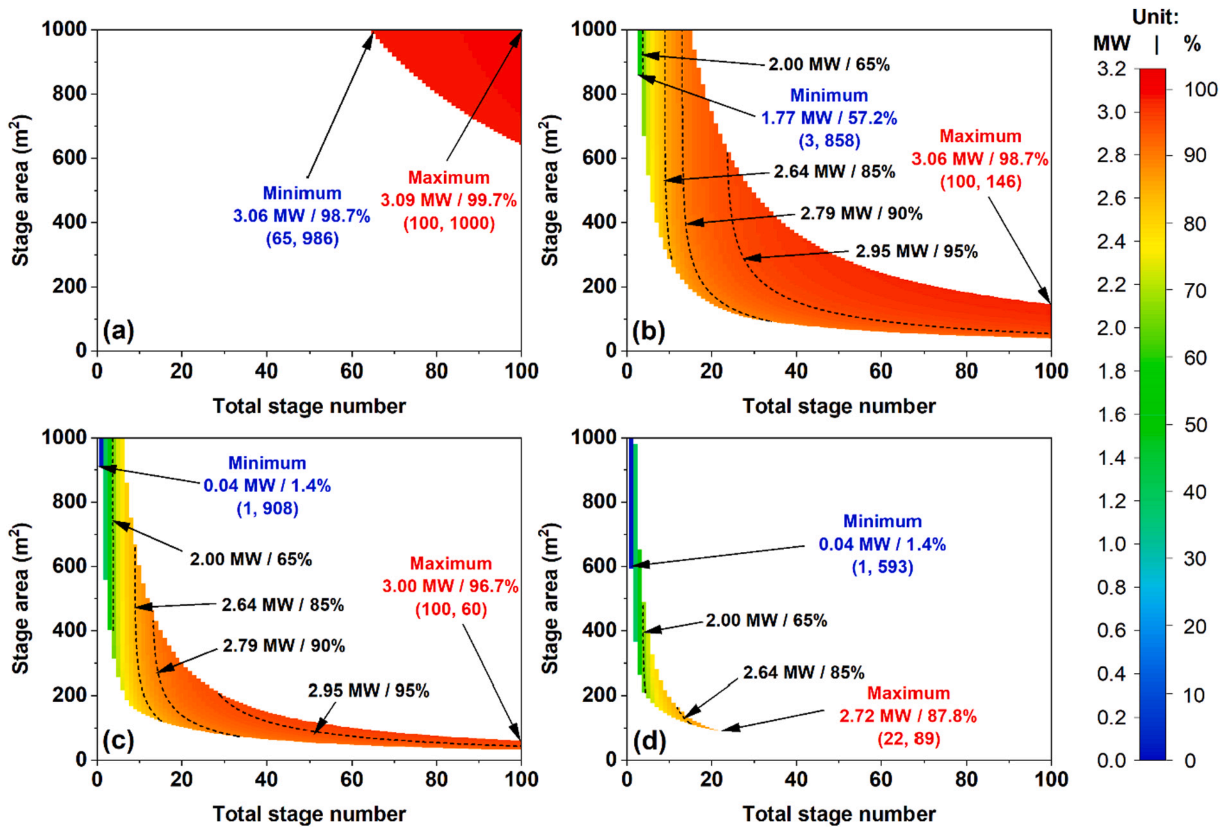

Fig. 7. Total heat release rate and RTE in PES mode with respect to total stage number N and stage area A, with different HTF tube-side velocities v_{tube}: (a) 0.8 m/s, (b) 5 m/s, (c) 10 m/s, and (d) 15 m/s.

number, meaning that it is not useful to keep increasing the stage area A further in order to improve the total heat release rate in the CHP mode. For electricity generation, the critical stage areas for the total stage numbers of 10, 15 and 20 are 500 m^2, 460 m^2 and 430 m^2; for heating, the critical stage areas for the total stage numbers of 10, 15 and 20 are 430 m^2, 390 m^2 and 360 m^2; and for the CHP mode, the critical stage areas for the total stage numbers of 10, 15 and 20 are 410 m^2, 370 m^2 and 350 m^2.

In Fig. 9(a), as the total stage number N increases, the total heat release rates for electricity generation, heating and both purposes all tend to approach to each other for different stage areas and to approach their corresponding limits. However, in Fig. 9(b), the limits of the corresponding total heat release rates are determined by the total stage number N, meaning that once the total stage number N is fixed, the maximum of the total heat release rate in the CHP mode is irrespective of how the stage area changes. The limits for the total heat release rate in the CHP mode are 2.93 MW, 3.00 MW and 3.03 MW when the total stage numbers N are 10, 15 and 20, respectively. To some extent, it can be concluded that the total stage number N plays a greater role than the stage area A in the design of the CLHS.

The stage area A is a key design parameter that characterises the design of the heat store arrangement, while the total area A_{tot} (sum of all the stage areas A, which is $A \times N$ in this study) can be regarded as a performance indicator that determines the overall size and capital cost of the store. Fig. 10 shows the total heat release rate and RTE as a function of the total stage number N and total area A_{tot} in both PES and CHP modes for HTF tube-side velocities v_{tube} of 5 m/s and 10 m/s. In Fig. 10(a), when the heat store operates in the PES mode with the HTF tube-side velocity being 5 m/s, it is observed that the total heat release rate and RTE increase with the total stage number N and total area A_{tot}, with the total areas A_{tot} corresponding to the highest and lowest total heat release rate and RTE being 14600 m^2 and 2570 m^2, respectively. Contour lines representing RTE values of 85 %, 90 % and 95 % are also marked. To obtain these efficiencies with a smaller total area A_{tot} (also a lower capital cost), more stages are required, which leads to added cost/complexity of the CLHS. When the RTE is 85 %, the total area A_{tot} drops to 2880 m^2 with the total stage number $N = 11$. In Fig. 10(b), when the HTF tube-side velocity v_{tube} is 10 m/s, the valid region of the total stage number N and total area A_{tot} reduces, and the total areas A_{tot} for the highest and lowest total heat release rate and RTE are 6000 m^2 and 910 m^2.

Turning to the CHP mode, the total heat release rate and RTE are improved thanks to the multi-energy supply. In Fig. 10(c), a RTE as high as 100 % is achieved, but the corresponding total area A_{tot} is greater than 12100 m^2, making the store less economically attractive. RTE values of 85 % and 90 % are obtained when a total of four and six stages are deployed, with the smallest total areas of 2730 m^2 and 2810 m^2, respectively. For the RTE of 95 %, the total stage number N ranges from 11 to 17 with a total area A_{tot} from 10000 m^2 to 3040 m^2. In Fig. 10(d), the HTF tube-side velocity v_{tube} is 10 m/s again and the valid region reduces. The total areas A_{tot} for the highest and lowest total heat release rate and RTE are 6010 m^2 and 910 m^2. The smallest total areas for RTEs of 85 % and 90 % are 1280 m^2 and 1430 m^2, respectively. For a RTE of 95 %, the range of total stage numbers N extends to 11–22 with the total area A_{tot} decreasing from to 6020 m^2 to 2150 m^2. In summary, to maintain a specific high thermodynamic performance, the total stage number N and total area A_{tot} should be determined by taking the capital cost and complexity of the CLHS into consideration simultaneously.

(2) Temperature and heat release rate distributions

During discharging, the melting temperature in each stage is the same as that of the charging process and the outlet temperature is calculated from Eq. (10). The heat release rates in each stage for

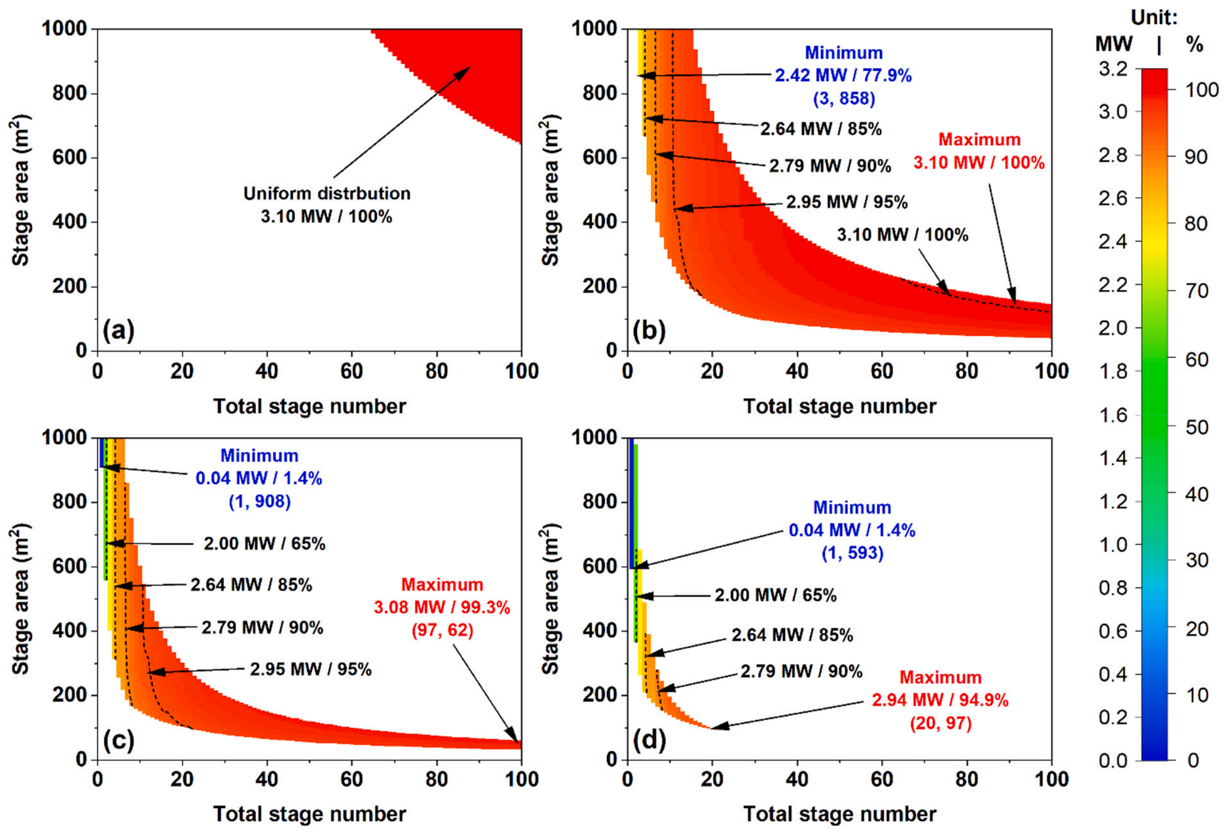

Fig. 8. Total heat release rate and RTE in CHP mode with respect to total stage number N and stage area A, with different HTF tube-side velocities v_{tube}: (a) 0.8 m/s, (b) 5 m/s, (c) 10 m/s, and (d) 15 m/s.

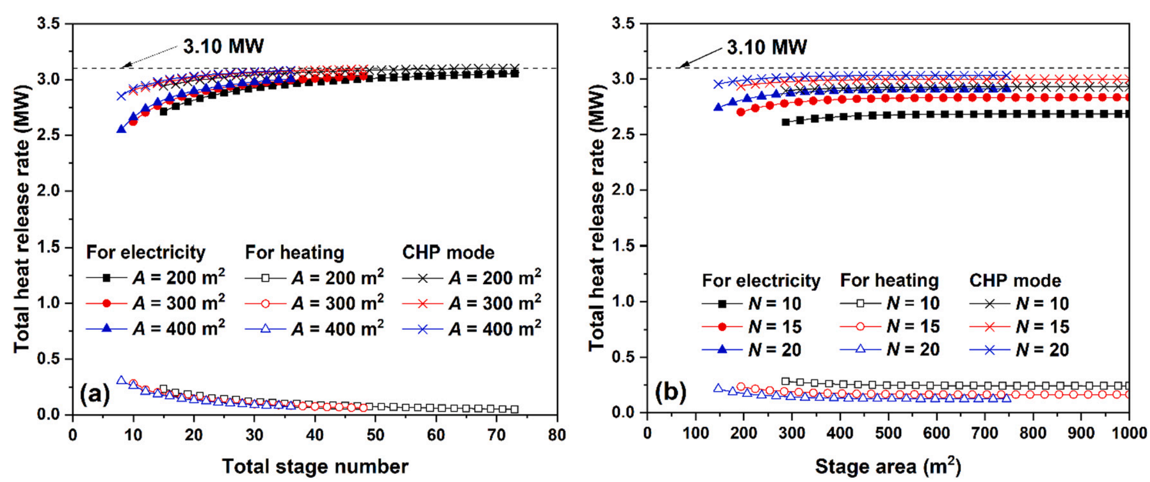

Fig. 9. Total heat release rate in CHP mode as a function of total stage number and stage area: (a) total stage number N varies from 1 to 80 and stage areas A of 200 m^2, 300 m^2 and 400 m^2 are considered, and (b) stage area A changes from 10 m^2 to 1000 m^2 and total stage numbers N = 10, 15 and 20 are investigated. HTF tube-side velocity v_{tube} is 5 m/s in all cases.

electricity generation, heating and the CHP mode are obtained by Eqs. (11), (12) and (13). In Fig. 11, the temperature and heat release rate distributions in each stage during discharging are given when the total stage numbers N are 10, 15 and 20. The stage area A is 300 m^2 and the HTF tube-side velocity v_{tube} is 5 m/s.

In Fig. 11(a), the outlet temperature in each stage increases along the HTF flow direction. Since the PCM melting temperature range widens when increasing the total stage number N, a higher HTF outlet temperature from the store can be obtained. The HTF outlet temperatures are 693 K, 719 K and 732 K, when the total stage numbers N are 10, 15 and 20. A larger total stage number N can also reduce the temperature difference between the HTF and PCM in each stage, and decrease the thermodynamic loss caused by irreversible heat transfer. Specifically, the average LMTDs over the stages are 15 K, 11 K and 8 K, when the total stage numbers N are 10, 15 and 20. In Fig. 11(b), heat release rates for electricity generation and direct heating are shown. For electricity generation, the heat release rate in each stage increases along the HTF flow direction and a uniform distribution is associated with a larger total stage number N. The heat release rate in each stage is distributed within the ranges of 28–410 kW, 32–288 kW and 35–222 kW when the total

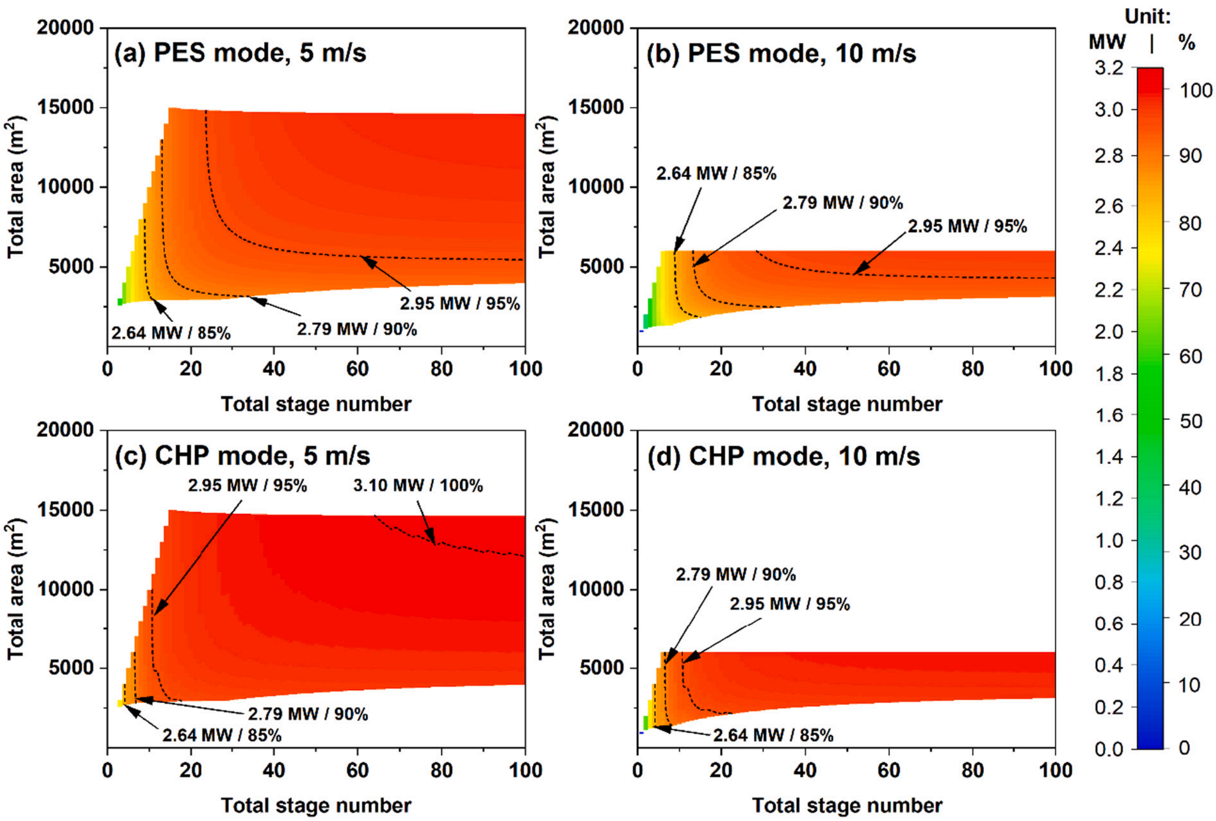

Fig. 10. Total heat release rate and RTE in different operational modes with respect to total stage number N and total area A_{tot}, with different HTF tube-side velocities v_{tube}: (a) PES mode and 5 m/s, (b) PES mode and 10 m/s, (c) CHP mode and 5 m/s, and (d) CHP mode and 10 m/s.

stage numbers N are 10, 15 and 20. Multi-grade thermal energy remains unused in each stage, which can be used for heating. In the last few stages, the remaining heat is not considered for direct heating purposes because the melting temperatures are below 353 K. The remaining heat is more uniformly distributed in a broader temperature range with a larger total stage number N, which is beneficial to the end-users for thermal energy. The heat release rate in each stage is distributed in the ranges of 25–47 kW, 11–22 kW and 6–12 kW when the total stage numbers N are 10, 15 and 20.

The temperature and heat release rate distributions through the CLHS when the stage areas A are 200 m^2, 300 m^2 and 400 m^2 are shown in Fig. 12. The total stage number N is 15 and the HTF tube-side velocity v_{tube} is 5 m/s. In Fig. 12(a), the HTF outlet temperature in each stage increases along the HTF flow direction and the HTF outlet temperature of the store increases when using a larger stage area A. More specifically, the HTF outlet temperatures of the store are 707 K, 719 K and 723 K, when the stage areas A are 200 m^2, 300 m^2 and 400 m^2. As the stage area A increases, the HTF outlet temperature in each stage tends to be higher and approaches the melting temperature in each stage, leading the average LMTD over the stages to be 16 K, 11 K and 8 K, for stage areas A of 200 m^2, 300 m^2 and 400 m^2. In Fig. 12(b), the heat release rate for electricity generation in each stage can be improved by a larger stage area A, while the heat release rate for heating in each stage decreases with the stage area A. In the last three stages, the melting temperatures

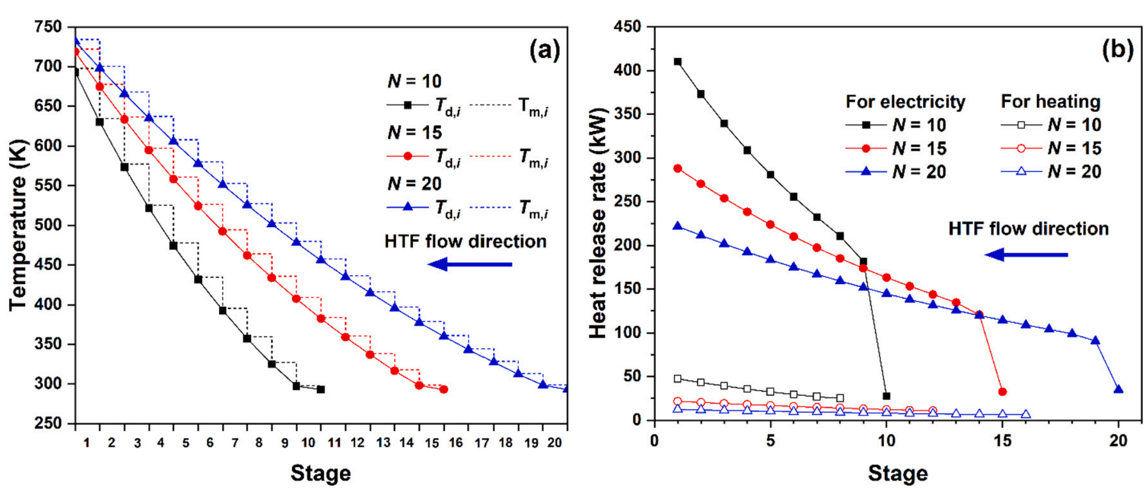

Fig. 11. Characteristics of each stage in CLHS during discharging: (a) melting and HTF outlet temperatures, and (b) heat release rate. Stage area A is 300 m^2, HTF tube-side velocity v_{tube} is 5 m/s and total stage numbers N = 10, 15 and 20 are considered.

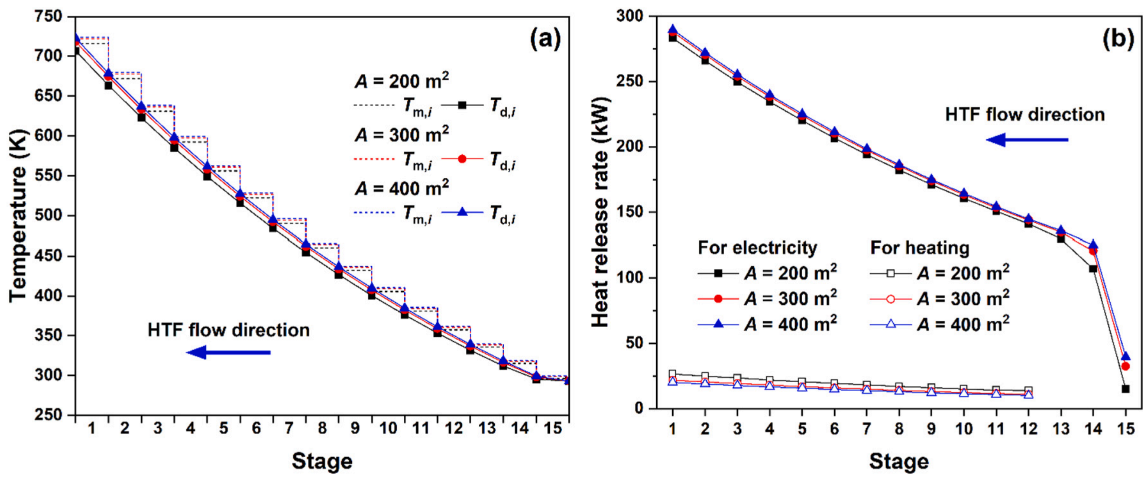

Fig. 12. Characteristics of each stage in CLHS during discharging: (a) melting and HTF outlet temperatures, and (b) heat release rate. Total stage number N is 15, HTF tube-side velocity v_{tube} is 5 m/s and stage areas A = 200 m^2, 300 m^2 and 400 m^2 are considered.

are all below 353 K under the investigated stage areas, and the stored heat cannot be considered for direct heating. For electricity generation, the heat release rate in each stage is distributed in the wide ranges of 15–283 kW, 32–288 kW and 40–290 kW when the stage areas A are 200 m^2, 300 m^2 and 400 m^2; for heating, the corresponding heat release rate in each stage is distributed in the narrow ranges of 14–27 kW, 11–22 kW and 10–20 kW when the stage areas A are 200 m^2, 300 m^2 and 400 m^2.

3.2. HTF tube-side velocity

In Section 3.1, it was found that beyond the total stage number N and stage area A, the HTF tube-side velocity v_{tube} also plays an important role in the total heat storage and release rates as well as the RTE, so it is vital to understand the effect of the HTF tube-side velocity on the thermodynamic performance of the CLHS. Fig. 13 gives the maxima, averages and minima of the total heat release rate and RTE in both PES and CHP modes for HTF tube-side velocities v_{tube} from 0.8 m/s to 20 m/s. The total stage number N and stage area A range from 1 to 100 and from 10 m^2 to 1000 m^2, respectively. According to the CLHS model described in Section 2.1, the HTF mass flow rate, HTF specific heat capacity and HTF inlet and outlet temperatures of the store are fixed at 12.5 kg/s, 524 J/(kg·K), 773 K and 300 K, respectively, such that the total heat storage rate of the whole store is not affected by the HTF tube-side velocity and is fixed at 3.10 MW.

The maxima of the total heat release rates in the PES and CHP modes stay within 3.02–3.09 MW and 3.09–3.10 MW, respectively, until the HTF tube-side velocity v_{tube} reaches 9.1 m/s and then decreases to 1.95 MW and 2.58 MW when the HTF tube-side velocity v_{tube} increases to 20 m/s. The maxima of the RTE vary with the HTF tube-side velocity v_{tube} similarly to the corresponding total heat release rates due to the constant total heat storage rates and decrease from 99.7 % to 62.8 % for the PES mode, and from 100 % to 83.3 % for the CHP mode. The maxima of the total heat release rate and RTE are found to be improved by an average of 6.5 % within the investigate range of the HTF tube-side velocity v_{tube} when operating in the CHP mode.

The minima of the total heat release rates in the PES and CHP modes drop in step from 3.06 MW to 0.03 MW and from 3.10 MW to 0.03 MW, respectively. Five distinct step changes are observed in these results: 3.1–3.6 m/s, 3.6–4.3 m/s, 4.3–5.8 m/s, 5.8–9.1 m/s and 9.1–20 m/s. The total heat release rates in the PES mode in the first four ranges are 2.27 MW, 2.08 MW, 1.77 MW and 1.23 MW with the RTE being 73.2 %, 67.0 %, 57.2 % and 39.8 %, while the corresponding heat release rates and RTEs in the CHP mode are 2.73 MW and 88.2 %, 2.62 MW and 84.5 %, 2.42 MW and 77.9 %, 1.95 MW and 63.1 %. When the HTF tube-side velocity v_{tube} is higher than 9.1 m/s, the minima of the total heat release rates and RTEs in the PES and CHP modes approach zero, because the single-stage store starts to satisfy the restrictions of PCM melting temperature, volume and HTF pressure loss.

The average total heat release rate and RTE within the investigated range of total stage number N and stage area A in the PES and CHP modes are also shown, which can represent the distribution of the total heat release rate and RTE obtained at most pairs of total stage number N and stage area A. The average total heat release rate and RTE in the PES mode decrease from 3.08 MW to 0.53 MW and from 99.2 % to 17.0 % as the HTF tube-side velocity v_{tube} increases from 0.8 m/s to 20 m/s. The corresponding average heat release rate and RTE in the CHP mode increase to the ranges of 0.80–3.10 MW and 25.5–100 % with an average improvement of 18 %.

Fig. 14 shows the total stage number N and total area A_{tot} corresponding to the maxima and minima of the total heat release rate and RTE in both PES and CHP modes with HTF tube-side velocities v_{tube} ranging from 0.8 m/s to 20 m/s. In Fig. 14(a), the corresponding total stage numbers N for the minima of the total heat release rate and RTE are the same for both PES and CHP modes, although we recall that when the HTF tube-side velocity v_{tube} is 0.8 m/s the total heat release rate and RTE for the CHP mode reach their maximum values of 3.10 MW and 100 % within the entire valid region and no minima exist (see Fig. 8(a)). The

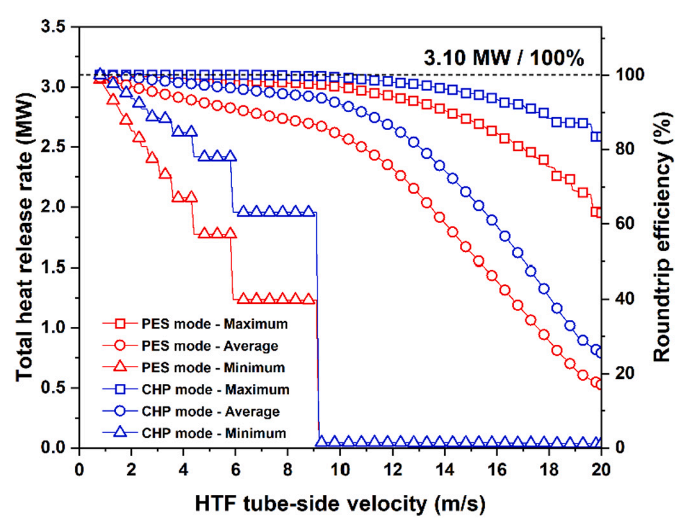

Fig. 13. Maximum, average and minimum of total heat release rate and RTE in PES and CHP modes as a function of HTF tube-side velocity v_{tube}. The maximum, average and minimum are calculated based on the results within the corresponding valid region of total stage number N and stage area A.

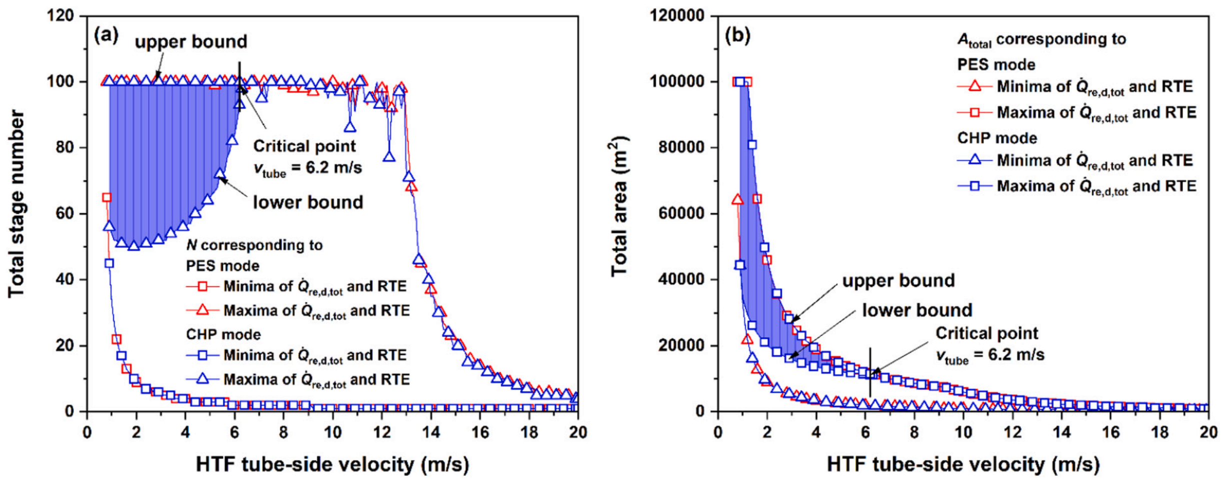

Fig. 14. Characteristics corresponding to the total heat release rate and RTE maxima and minima in PES and CHP modes as a function of HTF tube-side velocity v_{tube}: (a) total stage number N, and (b) total area A_{tot}.

corresponding total stage number N associated with the worst thermodynamic performance decreases with the HTF tube-side velocity v_{tube} and remains below 6 for HTF tube-side velocities $v_{tube} > 3$ m/s. For the best thermodynamic performance, the total stage numbers N for these two operational modes overlap when the HTF tube-side velocity $v_{tube} >$ 13.2 m/s. It is worth noting that there exists a critical velocity of 6.2 m/s in the CHP mode below which the total stage number N lies within a range, because the highest RTE of 100 % can be achieved within a valid region rather than an individual pair (e.g., Figs. 8(b) and 10(c)). Below the critical velocity, it is possible to obtain the optimal performance by deploying much fewer stages in the CHP mode.

Due to the relation between the total area, size and capital cost of the thermal stores, it is important to understand the variation of the total area A_{tot} of the store with the HTF tube-side velocity v_{tube}. In Fig. 14(b), the corresponding total areas A_{tot} associated with the maximum and minimum total heat release rate and RTE are shown for the range of HTF tube-side velocities v_{tube}. For the best thermodynamic performance (i.e., maximum total heat release rate and RTE), the total areas A_{tot} are higher than for a lower thermodynamic performance, which suggests that there exists a trade-off between thermodynamic performance and size/cost. Furthermore, the thermodynamic performance of both operational modes decreases as the HTF tube-side velocity v_{tube} increases. Above the critical velocity of 6.2 m/s, the two total areas A_{tot} differ little from each other. When the HTF tube-side velocity drops below the critical velocity, the highest RTE of 100 % can be attained within a range of total area A_{tot} in the CHP mode, which is consistent with the results of total stage number N shown in Fig. 14(a). The lower bound of the total area A_{tot} in CHP mode is the most promising in the context of achieving good thermodynamic performance at lower HTF tube-side velocities as the cost can be reduced.

3.3. Comparison with packed-bed and liquid sensible-heat stores

As PBSHSs and LSHSs have been recognised as viable options in PTES systems, a comparison of CLHSs with the performance of these alternatives is necessary to understand the thermodynamic potential and to evaluate the feasibility of CLHSs in PTES applications. The modelling methodology employed for PBSHS and LSHS performance predictions is described in the Appendix. For comparison, argon is used as a common HTF for the three types of heat stores and the operating conditions, including the HTF inlet and outlet temperatures during charging, HTF inlet temperature during discharging, operating pressure, HTF flow rate and charging/discharging time, are kept the same. In the PBSHS model, the length-to-diameter ratio ξ and volume design factor η are the two parameters that determine the actual packed-bed store size. In this study, the length-to-diameter ratio ξ and volume design factor η are set to range from 1 to 10 and from 1 to 2, respectively. A heat exchanger is also added to the PBSHS in series to discharge the excess heat. The lowest HTF tube-side velocity v_{tube} is obtained by Eqs. (25), (26) and (27) when the tube pitch d_{tp} equals the outer tube diameter d_o and is calculated to be greater or equal to 3.4 m/s. Here, the HTF tube-side velocity is set to range from 3.4 m/s to 20 m/s. In the LSHS model, two sets of heat stores are needed to cover the whole operating temperature and each heat store consists of two liquid stores and a heat exchanger. The investigated variables here are the HTF temperature at the connection point of heat exchangers during charging $T_{cp,f,c}$ and HTF tube-side velocity v_{tube}. In this study, according to the working temperature ranges of liquid working fluids (WFs), the HTF temperature at the connection point of heat exchangers during charging $T_{cp,f,c}$ ranges from 406 K to 619 K, while the HTF tube-side velocity v_{tube} is the same as the heat exchanger in the PBSHS and ranges from 3.4 m/s to 20 m/s.

The total CLHS, PBSHS and LSHS heat storage rates are plotted in Fig. 15. For the CLHS and LSHS, the total heat storage rates are both equal to 3.10 MW irrespective of changes to the variables (total stage number N, stage area A and HTF tube-side velocity v_{tube} for the CLHS; HTF temperature at the connection point of heat exchangers during charging $T_{cp,f,c}$ and HTF tube-side velocity v_{tube} for the LSHS), because the HTF flow rate, HTF specific heat capacity and HTF inlet and outlet temperatures of the store are fixed at 12.5 kg/s, 524 J/(kg·K), 773 K and 300 K, as described in Section 2.1. For the PBSHS, the average of the total heat storage rate is chosen because the HTF outlet temperature of the packed bed during charging increases above the environmental temperature when the thermal front reaches the outlet of the packed bed, and the excess heat has to be rejected to the environment through an additional heat exchanger. In this case, the average of the total heat storage rate for the PBSHS is found to vary from 2.78 MW and 3.10 MW, but reaches the limiting value of 3.10 MW when the volume design factor η is greater or equal to 1.7. The corresponding maxima and minima are obtained when the pair of length-to-diameter ratio ξ and volume design factor η are (1, 2) and (1, 1), respectively.

The total storage rates of the PBSHS when the length-to-diameter ratios ξ are 1, 5, 10 and volume design factors η are 1, 1.7, 2 are also selected and marked in Fig. 15. The total storage rate is lower when the volume design factor η is 1, and the total heat storage rate increases with the length-to-diameter ratio ξ when the volume design factor η is smaller. However, when the volume design factor η reaches 1.7 or 2, the total heat storage rate shows only a negligible change as the length-to-diameter ratio ξ increases. In addition, when the volume design factor η is smaller than 1.7, the total heat storage rate increases with the volume design factor η. Overall, it is found that the total heat storage rate of

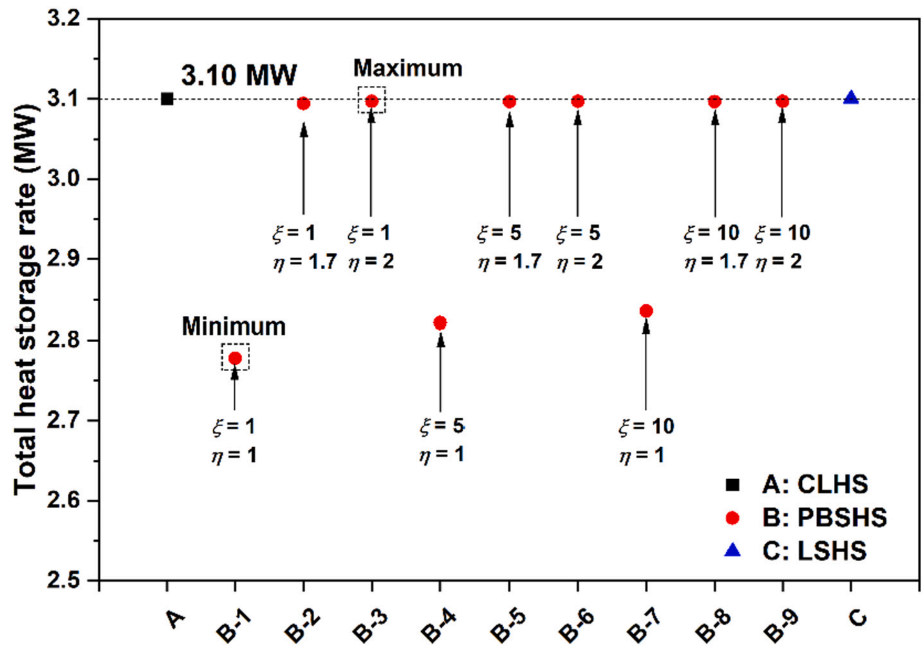

Fig. 15. Total heat storage rates of CLHS, PBSHS and LSHS. A: CLHS, $1 \leq N \leq 100$, $10\ m^2 \leq A \leq 1000\ m^2$, and $0.8\ m/s \leq v_{tube} \leq 20\ m/s$. B: PBSHS, $1 \leq \xi \leq 10$ and $1 \leq \eta \leq 2$. C: LSHS, $406\ K \leq T_{cp,f,c} \leq 619\ K$ and $3.4\ m/s \leq v_{tube} \leq 20\ m/s$. For CLHS and LSHS, the total heat storage rate is constant and not affected by the variables.

the CLHS is comparable to those of the PBSHS and LSHS if the total stage number N, stage area A and HTF tube-side velocity v_{tube} are selected within the valid region.

The total heat release rate and RTE of the CLHS, PBSHS and LSHS are shown in Fig. 16. For the CLHS, since the total stage number N and stage area A range from 1 to 100 and from $10\ m^2$ to $1000\ m^2$, corresponding to a wide range of the total heat release rate and RTE values at a specific HTF tube-side velocity v_{tube}, only the maxima and minima at specific HTF tube-side velocities v_{tube} of 5 m/s, 10 m/s and 15 m/s are marked in the figure.

The operation mode affects the total heat release rate and the RTE. In the PES mode, the total heat release rate ranges widely from 0.03 MW to 3.09 MW, indicating that not all the stored heat is used for electricity generation. More specifically, the ranges are 3.06–3.09 MW, 1.77–3.06 MW, 0.04–3.00 MW, 0.04–2.72 MW and 0.03–1.95 MW for HTF tube-side velocities v_{tube} of 0.8 m/s, 5 m/s, 10 m/s, 15 m/s and 20 m/s. The corresponding ranges increase to 3.10 MW, 2.42–3.10 MW, 0.04–3.08 MW, 0.04–2.94 MW and 0.03–2.58 MW in the CHP mode. The lower total heat release rate and RTE are obtained at higher HTF tube-side velocities when the single-stage store is deployed. If the single-stage store is neglected, the lowest RTE improves to 36 % for the PES mode and 62 % for the CHP mode. In all cases, the difference between the maxima and minima for any given HTF tube-side velocity is associated with a different total store area A_{tot}; the maxima with larger areas. Therefore, it can be concluded that technically the higher end of achievable total heat storage rates and RTEs of CLHSs is comparable to the performance of PBSHSs and LSHSs, however, the economics of these designs will need to be compared to lower cost alternative CLHSs designs that may not achieve the best thermodynamic performance.

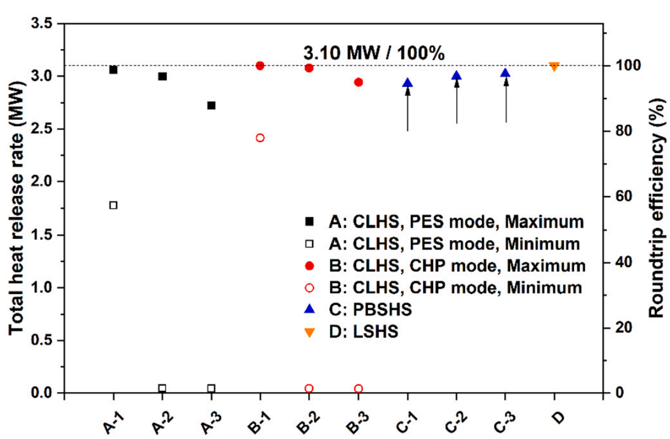

Fig. 16. Total heat release rates and RTEs of CLHS, PBSHS and LSHS. A: CLHS, PES mode, $1 \leq N \leq 100$, $10\ m^2 \leq A \leq 1000\ m^2$, $v_{tube} = 5$ m/s (A-1), 10 m/s (A-2) and 15 m/s (A-3). B: CLHS, CHP mode, $1 \leq N \leq 100$, $10\ m^2 \leq A \leq 1000\ m^2$, $v_{tube} = 5$ m/s (B-1), 10 m/s (B-2) and 15 m/s (B-3). C: PBSHS, $(\xi, \eta) = (1, 1.3)$ (C-1), (5, 1.3) (C-2), and (10, 1.3) (C-3). D: LSHS, $406\ K \leq T_{cp,f,c} \leq 619\ K$ and $3.4\ m/s \leq v_{tube} \leq 20\ m/s$.

For the PBSHS, the average total heat release rate is found to be between 2.80 MW and 3.02 MW with the RTE ranging from 90 % to 98 %. The minima are achieved when the length-to-diameter ratio ξ is 1 and volume design factor η is 1, while the maxima are reached when the length-to-diameter ratio ξ is 10 and volume design factor η is 1.3. It is also found that the highest total heat release rate and RTE are achieved when the volume design factor η is 1.3 at a constant length-to-diameter ratio ξ. Moreover, a larger length-diameter ratio ξ is beneficial for the higher total heat release rate and RTE. The optimal results obtained when the length-diameter ratios ξ are 1, 5 and 10 are presented in Fig. 16. For the LSHS, the total heat release rate remains at 3.10 MW and the RTE is 100 %. It is found, therefore, that the heat release rate and RTE of CLHSs can vary within a range by adjusting the total stage number N, stage area A and HTF tube-side velocity v_{tube}, and that their higher values are comparable to equivalent PBSHSs and LSHSs.

Finally, we consider the pressure losses in CLHSs, which are relatively low according to Assumption (v) in the model described in Section 2.1, as they are restricted to be no more than 10 % of the initial operating pressure, such that the maximum pressure loss in this case is below 0.10 MPa. It is found that the pressure gradient is related to the HTF tube-side velocity and changes from 10 Pa/m to 2270 Pa/m when the HTF tube-side velocity v_{tube} increases from 0.8 m/s to 20 m/s. For the PBSHS, the total pressure loss includes the pressure loss in the packed bed and that in the heat exchanger. The total pressure loss ranges from 445 Pa to 1.17×10^5 Pa within the investigated ranges of length-to-diameter ratio ξ, volume design factor η and HTF tube-side velocity v_{tube}. The maximum pressure loss is higher than the limit of 0.1 MPa and

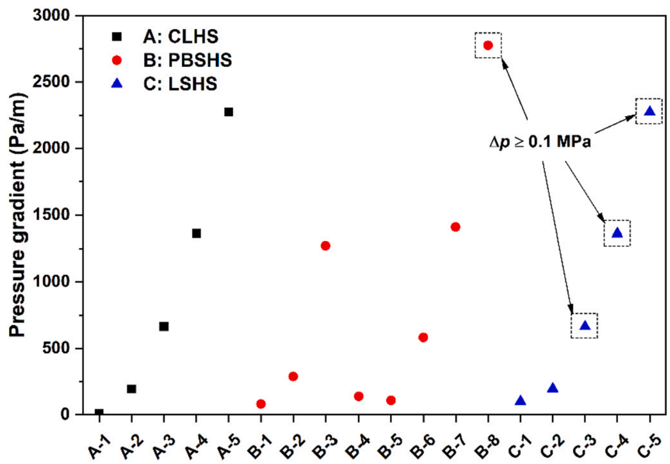

Fig. 17. Pressure gradient of CLHS, PBSHS and LSHS. A: CLHS, $1 \le N \le 100$, $10\ \text{m}^2 \le A \le 1000\ \text{m}^2$, $v_{\text{tube}} = 0.8$ m/s (A-1), 5 m/s (A-2), 10 m/s (A-3), 15 m/s (A-4) and 20 m/s (A-5). B: PBSHS, (ξ, η, v_{tube}) = (1, 2, 3.4 m/s) (B-1), (1, 2, 10 m/s) (B-2), (1, 2, 20 m/s) (B-3), (1, 1, 3.4 m/s) (B-4), (1, 1.5, 3.4 m/s) (B-5), (5, 2, 3.4 m/s) (B-6), (10, 2, 3.4 m/s) (B-7) and (10, 1, 20 m/s) (B-8). C: LSHS, 406 K $\le T_{\text{cp,f,c}} \le$ 619 K, $v_{\text{tube}} = 3.4$ m/s (C-1), 5 m/s (C-2), 10 m/s (C-3), 15 m/s (C-4) and 20 m/s (C-5). The pressure gradients that correspond to pressure losses above 0.1 MPa are marked by squares on the figure.

is achieved when the length-to-diameter ratio ξ is 10, volume design factor η is 1 and HTF tube-side velocity v_{tube} is 20 m/s, while the corresponding minimum is obtained when $\xi = 1$, $\eta = 2$ and $v_{\text{tube}} = 3.4$ m/s. The maximum and minimum of the pressure loss also correspond to the highest and lowest pressure gradients of 80 Pa/m and 2770 Pa/m. For the LSHS, the pressure loss ranges from 1.58×10^4 Pa when the HTF temperature at the connection point of heat exchangers during charging $T_{\text{cp,f,c}}$ is 406 K and the HTF tube-side velocity v_{tube} is 3.4 m/s, to 1.70×10^6 Pa when $T_{\text{cp,f,c}}$ is 619 K and v_{tube} is 20 m/s, with most designs being above 0.10 MPa. The pressure gradient is closely related to the HTF tube-side velocity and changes from 100 Pa/m when $v_{\text{tube}} = 3.4$ m/s to 2270 Pa/m when $v_{\text{tube}} = 20$ m/s. The pressure gradients exhibited by the three types of heat stores are compared in Fig. 17.

The pressure gradients in the CLHS are 10 Pa/m, 200 Pa/m, 660 Pa/m, 1360 Pa/m and 2270 Pa/m, respectively, when the HTF tube-side velocities v_{tube} are 0.8 m/s, 5 m/s, 10 m/s, 15 m/s and 20 m/s. The pressure gradient in the PBSHS ranges between 80 Pa/m and 2770 Pa/m, increasing with the length-diameter ratio ξ and the HTF tube-side velocity v_{tube}, and decreasing with the volume design factor η. The pressure gradients in the LSHS are found to be 100 Pa/m, 200 Pa/m, 660 Pa/m, 1360 Pa/m and 2270 Pa/m, respectively, when the HTF tube-side velocities v_{tube} are 3.4 m/s, 5 m/s, 10 m/s, 15 m/s and 20 m/s. Here, pressure gradients that correspond to a pressure loss above 0.1 MPa over the length of the store (indicated by squares in Fig. 17) should not be considered further. It can be concluded that the pressure loss and pressure gradient in the CLHS can be controlled comparable to those of the PBSHS and LSHS.

4. Conclusions

This paper presents results from an investigation into the thermodynamic feasibility of cascaded latent-heat stores, specifically exploring their deployment in pumped-thermal energy storage applications. A thermodynamic model of cascaded latent-heat stores is established based on exergy and entropy generation optimisation, and the melting temperature in each stage is found to be arranged in a decreasing geometric progression along the heat transfer fluid flow direction. The effects of the heat store design (total stage number N and stage area A) and of the HTF tube-side velocity v_{tube} on the heat storage and release rates (both of the whole store and of each stage) as well as the roundtrip efficiency (RTE) are considered. Both a pure electricity-storage (PES) mode and a combined heating and power (CHP) mode are investigated, which gives the PTES system a broader potential to transform from a pure electricity storage system to an energy management system supplying power along with multi-grade heat and cold, while also recovering external multi-grade waste heat and/or cold, if available, in order to promote further performance benefits. The thermodynamic performance of cascaded latent-heat stores is compared to equivalent packed-bed and liquid sensible-heat stores.

The heat store design, which focuses here on the total stage number N and stage area A, does not affect the total heat storage rate of the whole store, but impacts the temperature and heat storage rate distributions in each stage during charging. By increasing the total stage number N, the melting temperature range can be widened, the temperature difference between the HTF and PCM in each stage can be decreased, and the heat storage rate in each stage can be adjusted to achieve a more uniform distribution. For different stage areas A, the HTF outlet temperatures in each stage are the same, while larger stage areas lead the melting temperatures in each stage to be closer to the corresponding outlet temperatures. During discharging, the total heat release rate and RTE show a similar variation due to the constant total heat storage rate in both PES and CHP modes. As the HTF tube-side velocity increases from 5 m/s to 15 m/s, the valid regions of the total stage number N and stage area A for the RTEs higher than 85 %, 90 % and 95 % are reduced significantly. The best-case RTE reduces from 98.7 % ($N = 100$, $A = 150\ \text{m}^2$) to 87.8 % ($N = 22$, $A = 90\ \text{m}^2$) for the PES mode and from 100 % (in a narrow region) to 94.9 % ($N = 20$, $A = 100\ \text{m}^2$) for the CHP mode. It is also found that single-stage stores are not suitable for this application given their very low efficiencies. In the CHP mode, the total heat release rate for electricity generation increases with the total stage number N and stage area A, while the total heat release rate for heating purposes changes in an opposite sense. The heat release rates for both electricity generation and direct heating in each stage are more uniformly distributed along the store length when the total stage number N is larger; the heat release rate for electricity generation is improved when using a larger stage area A, whereas the heat release rate for heating decreases. The total area A_{tot} is also considered, which directly determines the size, and therefore also affects the capital cost of the store. In order to maintain a high RTE (e.g., $\geq$90 %), though the capital cost can be reduced by deploying more stages, the total stage number N should also be taken into consideration as it is associated with the complexity as well as the costs of the CLHS. The present work, therefore, suggests that there exists a trade-off between thermodynamic performance and cost.

For the investigated ranges of total stage number and stage area, the total heat storage rate of the whole store is not affected by the HTF tube-side velocity and is also constant at 3.10 MW within the HTF tube-side velocity range 0.8–20 m/s. In contrast, the total heat release rate and the corresponding RTE lie within specific ranges with corresponding maxima, averages and minima that decrease with the HTF tube-side velocity, especially when the HTF tube-side velocity is greater than 9.1 m/s. The total heat release rate and RTE in the CHP mode are higher by an average of 18 % compared to those in the PES mode. The corresponding total stage numbers N and total areas A_{tot} for the best and worst thermodynamic performance also generally decrease with the HTF tube-side velocity v_{tube} and there is a critical velocity at 6.2 m/s for the CHP mode, below which the total stage number N and the total area A_{tot} for the best performance are in certain ranges rather than an individual pair of values. This may provide solutions for low-velocity cases to achieve high performance, simple configuration and low capital cost.

In the investigated cases, and if we ignore the single-stage store case, the cascaded latent-heat stores have maximum (best case) RTEs that range from 62 % to 100 % when operating in the CHP mode, and a pressure loss gradient that ranges from 10 Pa/m to 2270 Pa/m, both of which are comparable to the packed-bed and liquid sensible-heat stores. It is noted, nevertheless, that although the best performing (in terms of total heat storage rates and RTEs) CLHS designs are comparable to the performance of packed-bed and liquid sensible-heat stores, the economics of these designs will need to be compared to alterative store designs that may not achieve the best thermodynamic performance but are, however, associated with lower costs. Therefore, it is concluded that cascaded latent-heat store may be feasible in Joule-Brayton cycle-based pumped-thermal energy storage systems for intelligent energy management that can provide power and multi-grade heat and cold at the same time if the costs can justify this decision.

CRediT authorship contribution statement

Yao Zhao: Conceptualization, Methodology, Software, Validation, Formal analysis, Investigation, Writing – original draft, Funding acquisition. **Jian Song:** Formal analysis, Investigation, Data curation, Writing – review & editing. **Changying Zhao:** Resources, Writing – review & editing, Supervision. **Yongliang Zhao:** Formal analysis, Investigation, Writing – review & editing. **Christos N. Markides:** Formal analysis, Investigation, Resources, Writing – review & editing, Visualization, Supervision, Project administration, Funding acquisition.

Declaration of competing interest

The authors declare that they have no known competing financial interests or personal relationships that could have appeared to influence the work reported in this paper.

Data availability

Data will be made available on request.

Acknowledgements

This work was supported by the National Natural Science Foundation of China (Grant No. 51906150) and the UK Engineering and Physical Sciences Research Council (EPSRC) [grant numbers EP/P004709/1, EP/R045518/1, and EP/S032622/1]. Data supporting this publication can be obtained on request from cep-lab@imperial.ac.uk. For the purpose of Open Access, the authors have applied a CC BY public copyright licence to any Author Accepted Manuscript version arising from this submission.

Appendix A

A.1. Packed-bed sensible-heat store

A.1.1. Physical description

As shown in Fig. 1, the solid particles are usually arranged randomly or uniformly in packed-bed sensible-heat stores (PBSHSs). During charging, HTF 1 usually flows through the porous media from the top to the bottom to reduce the effect of buoyancy-driven mixing and transfers heat to solid particles, while during discharging, HTF 1 flows from the bottom to the top and absorbs heat from the solid particles. Due to the large specific surface area, there exists a thermal front where heat transfer occurs between HTF 1 and solid particles along with significant temperature gradients. When the thermal front reaches the store bottom during charging, the outlet temperature of HTF 1 starts to increase. In order to maintain a constant outlet temperature, an additional heat exchanger is usually deployed to discharge the excess heat to the environment.

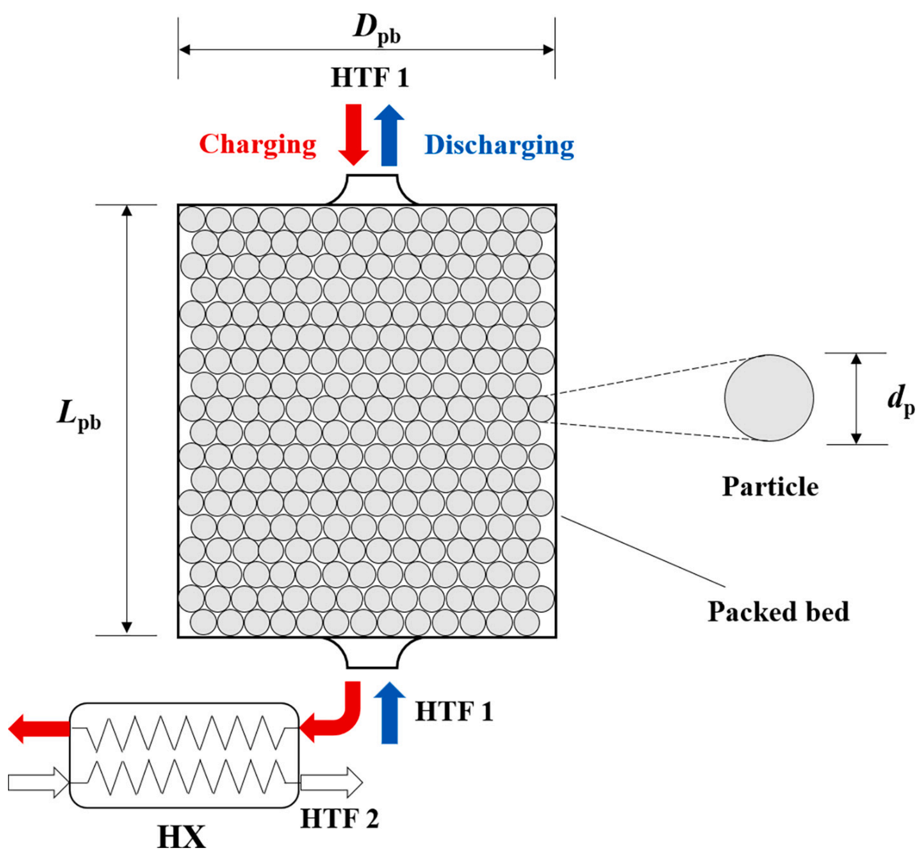

Fig. 1. Packed-bed sensible-heat store layout.

The volume of PBSHSs is calculated from:

$$V_{pb} = \frac{\dot{m}_f c_{p,f} \tau}{c_{p,s} \rho_s (1-\varepsilon)} \eta \tag{A1}$$

where $c_{p,f}$ is the specific heat capacity of HTF 1, $\dot{m}_f$ is the mass flow rate of HTF 1 during charging and discharging, τ is the charging/discharging time, $c_{p,s}$ is the specific heat capacity of the solid particles, ρ_s is the density of the solid particles, ε is the porosity, and η is the volume design factor.

Then the store length L_{pb} and store diameter D_{pb} can be further determined based on the volume:

$$L_{pb} = \left(\frac{4V_{pb}\xi^2}{\pi}\right)^{1/3} \tag{A2}$$

$$D_{pb} = \left(\frac{4V_{pb}}{\pi\xi}\right)^{1/3} \tag{A3}$$

where ξ is the length-diameter ratio of the PBSHS. Moreover, a counterflow shell-and-tube type heat exchanger is connected to the PBSHS for heat rejection. HTF 1 is on the tube side and HTF 2 is on the shell side.

The total length of the heat exchanger L_{HX} is also determined by its total heat transfer area A_{tot} as follows:

$$L_{HX} = \frac{A_{tot}}{n_{tube} \pi d_o} \tag{A4}$$

and the total heat transfer area of the heat exchanger A_{tot} is further calculated from:

$$A_{tot} = \frac{\dot{m}_f c_{p,f}\left(T_{cp,f,c}\big|_{t=\tau} - T_{out,f,c}\right)}{U \Delta T_M} \tag{A5}$$

where $T_{cp,f,c}$ is the temperature of HTF 1 at the connection point of the PBSHS and heat exchanger during charging, ΔT_M is the mean logarithmic temperature difference between HTF 1 and HTF 2, and U is the heat transfer coefficient, which is given by:

$$U = \frac{1}{d_o/(h_i d_i) + d_o ln(d_o/d_i)/(2k_{tube}) + 1/h_o} \tag{A6}$$

where d_i is the inner tube diameter, d_o is the outer tube diameter, h_i is the inner convective heat transfer coefficient, h_o is the outer convective heat transfer coefficient, k_{tube} is the thermal conductivity of the tube material, and the inner convective heat transfer coefficient h_i is calculated from:

$$h_i = \frac{k_f}{d_i} Nu = \frac{k_f}{d_i} \frac{(f/8)(Re-1000)Pr_f}{1 + 12.7(f/8)^{1/2}\left(Pr_f^{2/3} - 1\right)} \tag{A7}$$

where Nu is the Nusselt number, k_f is the HTF thermal conductivity, d_i is the inner tube diameter, f is the friction factor, Re is the Reynolds number, and Pr_f is the Prandtl number.

In Eq. (A7), f is determined from [37]:

$$f = \frac{1}{(0.79lnRe - 1.64)^2} = \frac{1}{\left(0.79ln\frac{\rho_f v_{tube} d_i}{\mu_f} - 1.64\right)^2} \tag{A8}$$

where ρ_f is the HTF density, v_{tube} is the HTF tube-side velocity, and μ_f is the HTF dynamic viscosity.

The outer convective heat transfer coefficient h_o is calculated using the Bell-Delaware method [34]:

$$h_o = j_i \frac{c_{p,ss} G_{ss}}{Pr_{ss}^{2/3}} \varphi \tag{A9}$$

where j_i is the ideal Colburn j factor for the shell side (HTF 2), $c_{p,ss}$ and Pr_{ss} are the specific heat capacity and Prandtl number of the shell-side fluid (HTF 2), φ is the viscosity correction factor, and G_{ss} is the mass flux of the shell-side fluid (HTF 2) and is related to the mass flow rate of the shell-side fluid (HTF 2) that can be obtained by energy balance in the heat exchanger. Here, several assumptions are also made: (i) fluid properties are constant, (ii) solid properties are also constant, except specific heat capacity, (iii) the temperature gradient inside particles is ignored, and (iv) heat dissipation to the environment is neglected.

In this study, the operating condition of the PBSHS and heat exchanger is the same as that of the cascaded latent heat store (CLHS), except that the inlet and outlet temperatures of the heat exchanger on the shell side (HTF 2) are assumed to be 293 K and 300 K, respectively. Since the inner shell diameter usually ranges from 0.06 m to 2 m, an intermediate value of 1 m is used for the heat exchanger and 3/4-in. O.D., 16 BWG (Birmingham Wire Gage) tubes are also used. The PBSHS and heat exchanger are also both made of stainless steel to avoid the creep risk in high-pressure and long-term applications at high temperatures [25]. Argon and air are used as HTF 1 and HTF 2, respectively, and 20 mm diameter Fe_3O_4 particles are filled as storage materials in the store with a porosity of 33 % due to their high energy density, easy availability and low costs. The thermophysical properties of air and Fe_3O_4 are given in Table 1 [36,46,47].

Table 1
Thermophysical properties of air and Fe_3O_4.

Specific heat capacity of air, $c_{p,ss}$	J/(kg·K)	1006.1
Density of air, ρ_{ss}	kg/m^3	1.20
Thermal conductivity of air, k_{ss}	W/(m·K)	0.03
Dynamic viscosity of air, μ_{ss}	Pa·s	1.82×10^{-5}
Specific heat capacity of Fe_3O_4, $c_{p,s}$	J/(kg·K)	$[104.21 + 178.51 \times (T / 1{,}000) + 10.62 \times (T / 1{,}000)^2 + 1.13 \times (T / 1000)^3 - 0.99 / (T / 1000)^2] / 0.23$
Density of Fe_3O_4, ρ_s	kg/m^3	5175
Thermal conductivity of Fe_3O_4, k_s	W/(m·K)	3.5

A.1.2. Mathematical models

According to the assumptions made in the physical model, a one-dimensional modified Schumann model is used to predict the flow and heat transfer characteristics in PBSHSs [7].

(1) Governing equations

$$\text{HTF 1}: \frac{\partial T_f}{\partial x} = \frac{(1-\varepsilon)S_v hAr(T_s - T_f)}{\dot{m}_f c_{p,f}} + \frac{\varepsilon Ar}{\dot{m}_f c_{p,f}}\left(\frac{\partial p}{\partial t} - \rho_f c_{p,f}\frac{\partial T_f}{\partial t}\right) \tag{A10}$$

$$\text{Solid particle}: \frac{\partial T_s}{\partial t} = \frac{S_v h(T_f - T_s)}{\rho_s c_{p,s}} + \frac{k_{eff}}{\rho_s c_{p,s}(1-\varepsilon)}\frac{\partial^2 T_s}{\partial x^2} \tag{A11}$$

where T_f and T_s are the temperatures of HTF 1 and solid particles, ε is the porosity of the packed bed, S_v is the packing surface area per unit volume, h is the fluid-to-solid heat transfer coefficient, Ar is the cross-section area of the packed bed, and k_{eff} is the effective thermal conductivity.

The heat transfer rate, heat storage rate and heat release rate of the whole PBSHS during charging and discharging are:

$$\dot{Q}_{tr,c,pb} = \dot{m}_f c_{p,f}(T_{in,f,c} - T_{out,f,c}) \tag{A12}$$

$$\dot{Q}_{st,c,pb} = \dot{m}_f c_{p,f}(T_{in,f,c} - T_{cp,f,c}) \tag{A13}$$

$$\dot{Q}_{tr,d,pb} = \dot{Q}_{re,d,pb} = \dot{m}_f c_{p,f}(T_{out,f,d} - T_{in,f,d}) \tag{A14}$$

where $T_{in,f,c}$ is the inlet temperature of HTF 1 during charging, $T_{out,f,c}$ is the outlet temperature of HTF 1 during charging, $T_{cp,f,c}$ is the temperature of HTF 1 at the connection point of the PBSHS and heat exchanger during charging, $T_{out,f,d}$ is the outlet temperature of HTF 1 during discharging, and $T_{in,f,d}$ is the inlet temperature of HTF 1 during discharging.

For the PBSHS, the roundtrip efficiency (RTE) is defined as the thermal energy output divided by the thermal energy input to the store as follows:

$$\text{RTE} = \frac{\int_0^\tau \dot{Q}_{re,d,pb} dt}{\int_0^\tau \dot{Q}_{tr,c,pb} dt} \tag{A15}$$

(2) Determination of key parameters

Here, the packing surface area per unit volume S_v, fluid-to-solid heat transfer coefficient h and effective thermal conductivity k_{eff} are calculated using the following equations [44]:

$$S_v = \frac{6}{d_p} \tag{A16}$$

$$h = Nu\frac{k_f}{d_p} = \frac{\left(2 + 1.1 Pr_f^{1/3} Re_f^{3/5}\right)k_f}{d_p} \tag{A17}$$

$$k_{eff} = \frac{1}{\varepsilon / k_f + (1-\varepsilon)/k_s} \tag{A18}$$

where d_p is the diameter of solid particles. The Ergun and Carman equations are used to estimate the pressure loss in the PBSHS [45,46]:

$$\text{Ergun equation}: \Delta p_{pb,Ergun} = \left(\frac{4.17}{Re_L} + 0.29\right)\frac{S_v(1-\varepsilon)\dot{m}_f^2}{\varepsilon^3 \rho_f Ar^2} L_{pb} \tag{A19}$$

$$\text{Carman equation}: \Delta p_{pb,Carman} = \left(\frac{5}{Re_L} + \frac{0.4}{Re_L^{0.1}}\right)\frac{S_v(1-\varepsilon)\dot{m}_f^2}{\varepsilon^3 \rho_f Ar^2} L_{pb} \tag{A20}$$

where the modified Reynolds number is:

$$Re_{\mathrm{L}} = \frac{\dot{m}_{\mathrm{f}}}{ArS_{\mathrm{v}}(1-\varepsilon)\mu_{\mathrm{f}}} \tag{A21}$$

The pressure loss on the tube side of the heat exchangers is estimated from:

$$\Delta p_{\mathrm{HX}} = \frac{f\rho_{\mathrm{f}}v_{\mathrm{tube}}^2}{2d_{\mathrm{i}}}L_{\mathrm{HX}} \tag{A22}$$

A.2. Liquid sensible-heat store

A.2.1. Physical description

In liquid sensible-heat stores (LSHSs) consisting of heat exchangers and liquid stores, during charging, liquid working fluids (WFs) flow from the low-temperature store to the high-temperature store and absorb heat from hot HTFs through heat exchangers; during discharging, the WFs flow reversely and release the heat to the cold HTFs. HTFs flows on the tube side, while the WFs is on the shell sides. In this study, the HTF temperature decreases from 773 K to 300 K during charging, making the working temperature range for liquid WFs wide, too. However, considering the solidification and decomposition temperatures of existing liquid WFs, it is difficult to cover the entire operating temperature range with only one kind of WFs, so at least two kinds of WFs are needed. For simplicity, two kinds of WFs, two sets of high-temperature and low-temperature stores and two sets of heat exchangers are deployed as illustrated in Fig. 2.

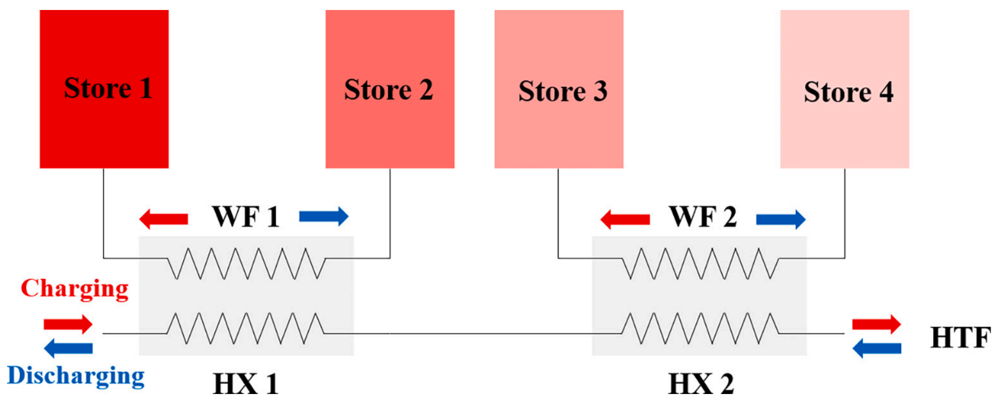

Fig. 2. Liquid sensible-heat store layout.

The total length of each heat exchanger L_{HX} is determined by the corresponding total heat transfer area A_{tot} as shown in Eq. (A4). The total heat transfer area A_{tot} is further calculated from:

$$A_{\mathrm{tot,HX1}} = \frac{\dot{m}_{\mathrm{f}}c_{\mathrm{p,f}}\left(T_{\mathrm{in,f,c}} - T_{\mathrm{cp,f,c}}\right)}{U_{\mathrm{HX1}}\Delta T_{\mathrm{M,HX1}}} \tag{A23}$$

$$A_{\mathrm{tot,HX2}} = \frac{\dot{m}_{\mathrm{f}}c_{\mathrm{p,f}}\left(T_{\mathrm{cp,f,c}} - T_{\mathrm{out,f,c}}\right)}{U_{\mathrm{HX2}}\Delta T_{\mathrm{M,HX2}}} \tag{A24}$$

where $T_{\mathrm{cp,f,c}}$ is the HTF temperature at the connection point of two heat exchangers during charging, U_{HX1} and U_{HX2} are the heat transfer coefficients of HX1 and HX2, $\Delta T_{\mathrm{M,HX1}}$ and $\Delta T_{\mathrm{M,HX2}}$ are the mean logarithmic temperature differences in HX1 and HX2. The heat transfer coefficients U_{HX1} and U_{HX2} and their outer convective heat transfer coefficient are given by Eqs. (A6) and (A9). The following assumptions are made to simplify the problem: (i) the thermophysical properties of HTFs and WFs are constant, (ii) the flows in the heat exchangers are balanced, i.e., observe $(\dot{m}c_{\mathrm{p}})_{\mathrm{f}} = (\dot{m}c_{\mathrm{p}})_{\mathrm{WF1}} = (\dot{m}c_{\mathrm{p}})_{\mathrm{WF2}}$, and (iii) the external insulation is enough such that heat dissipation to the environment is small enough to be ignored.

The operating conditions of the LSHS are the same as those of the CLHS. Counterflow shell-and-tube type heat exchangers with a shell diameter of 1 m and 3/4-in. O.D., 16 BWG (Birmingham Wire Gage) tubes are also adopted. They are also both made of stainless steel to avoid the creep risk in high-pressure and long-term applications at high temperatures [25]. The high-temperature and low-temperature stores are not considered here, because their parameters do not affect the flow and heat storage performance of the LSHS. HITEC XL salt is selected as the high-temperature WF (HT-WF), while Therminol 66 oil works as the lower-temperature WF (LT-WF). The thermophysical properties of WFs are shown in Table 2 [47–50].

Table 2
Thermophysical properties of working fluids.

Storage material	T_{min}, K	T_{max}, K	ρ, kg/m^3	c_{p}, J/(kg·K)	k, W/(m·K)	μ, mPa·s
HITEC XL salt	403	823	1960	1430	0.52	4.19
Therminol 66 oil	264	616	910	2070	0.11	1.20

A.2.2. Mathematical models

The ε-NTU method is adopted to calculate the heat transfer performance of LSHSs. Fig. 3 shows the temperature distributions of the HTF and WFs.

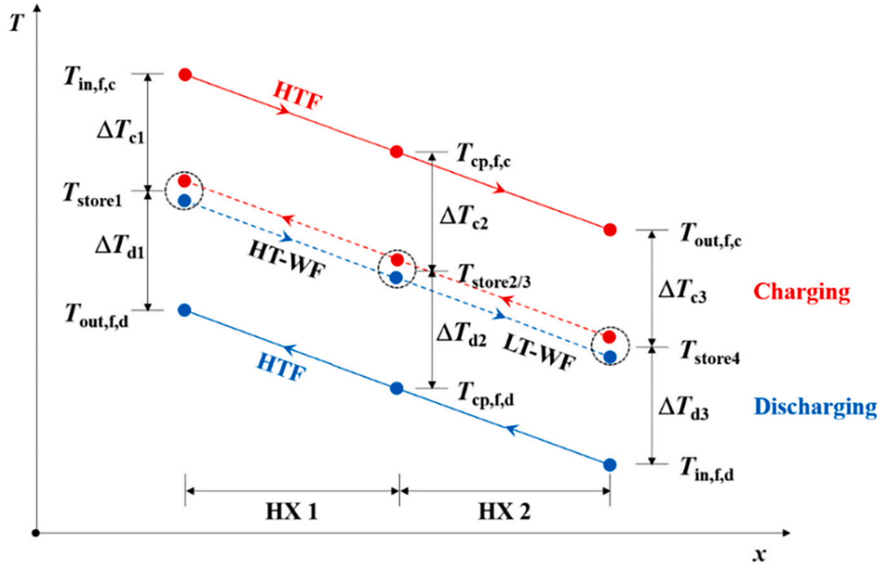

Fig. 3. Temperature distribution in liquid sensible-heat stores.

During charging, the effectiveness of HX1 and HX2 is:

$$\varepsilon_{\mathrm{HX1,c}} = \frac{(\dot{m}c_{\mathrm{p}})_{\mathrm{f}}\left(T_{\mathrm{in,f,c}} - T_{\mathrm{cp,f,c}}\right)}{(\dot{m}c_{\mathrm{p}})_{min,\mathrm{HX1}}\left(T_{\mathrm{in,f,c}} - T_{\mathrm{store2/3}}\right)} = \frac{(\dot{m}c_{\mathrm{p}})_{\mathrm{HT\text{-}WF}}\left(T_{\mathrm{store1}} - T_{\mathrm{store2/3}}\right)}{(\dot{m}c_{\mathrm{p}})_{min,\mathrm{HX1}}\left(T_{\mathrm{in,f,c}} - T_{\mathrm{store2/3}}\right)} \tag{A25}$$

$$\varepsilon_{\mathrm{HX2,c}} = \frac{(\dot{m}c_{\mathrm{p}})_{\mathrm{f}}\left(T_{\mathrm{cp,f,c}} - T_{\mathrm{out,f,c}}\right)}{(\dot{m}c_{\mathrm{p}})_{min,\mathrm{HX2}}\left(T_{\mathrm{cp,f,c}} - T_{\mathrm{store4}}\right)} = \frac{(\dot{m}c_{\mathrm{p}})_{\mathrm{LT\text{-}WF}}\left(T_{\mathrm{store2/3}} - T_{\mathrm{store4}}\right)}{(\dot{m}c_{\mathrm{p}})_{min,\mathrm{HX2}}\left(T_{\mathrm{cp,f,c}} - T_{\mathrm{store4}}\right)} \tag{A26}$$

During discharging, the effectiveness of HX1 and HX2 is:

$$\varepsilon_{\mathrm{HX1,d}} = \frac{(\dot{m}c_{\mathrm{p}})_{\mathrm{HT\text{-}WF}}\left(T_{\mathrm{store1}} - T_{\mathrm{store2/3}}\right)}{(\dot{m}c_{\mathrm{p}})_{min,\mathrm{HX1}}\left(T_{\mathrm{store1}} - T_{\mathrm{cp,f,d}}\right)} = \frac{(\dot{m}c_{\mathrm{p}})_{\mathrm{f}}\left(T_{\mathrm{out,f,d}} - T_{\mathrm{cp,f,d}}\right)}{(\dot{m}c_{\mathrm{p}})_{min,\mathrm{HX1}}\left(T_{\mathrm{store1}} - T_{\mathrm{cp,f,d}}\right)} \tag{A27}$$

$$\varepsilon_{\mathrm{HX2,d}} = \frac{(\dot{m}c_{\mathrm{p}})_{\mathrm{LT\text{-}WF}}\left(T_{\mathrm{store2/3}} - T_{\mathrm{store4}}\right)}{(\dot{m}c_{\mathrm{p}})_{min,\mathrm{HX2}}\left(T_{\mathrm{store2/3}} - T_{\mathrm{in,f,d}}\right)} = \frac{(\dot{m}c_{\mathrm{p}})_{\mathrm{f}}\left(T_{\mathrm{cp,f,d}} - T_{\mathrm{in,f,d}}\right)}{(\dot{m}c_{\mathrm{p}})_{min,\mathrm{HX2}}\left(T_{\mathrm{store2/3}} - T_{\mathrm{in,f,d}}\right)} \tag{A28}$$

where $(\dot{m}c_{\mathrm{p}})_{\mathrm{f}}$, $(\dot{m}c_{\mathrm{p}})_{\mathrm{HT\text{-}WF}}$ and $(\dot{m}c_{\mathrm{p}})_{\mathrm{LT\text{-}WF}}$ are the heat capacity rates of the HTF, high-temperature WF and low-temperature WF, $(\dot{m}c_{\mathrm{p}})_{\mathrm{min,HX1}}$ and $(\dot{m}c_{\mathrm{p}})_{\mathrm{min,HX2}}$ are the minimum heat capacity rates in HX1 and HX2, $T_{\mathrm{in,f,c}}$, $T_{\mathrm{cp,f,c}}$ and $T_{\mathrm{out,f,c}}$ are the HTF temperatures at the inlet, connection point and outlet of the LSHS during charging, $T_{\mathrm{in,f,d}}$, $T_{\mathrm{cp,f,d}}$ and $T_{\mathrm{out,f,d}}$ are the HTF temperatures at the inlet, connection point and outlet of the LSHS during discharging, and T_{store1}, $T_{\mathrm{store2/3}}$ and T_{store4} are the WF temperatures in Store 1, Stores 2 and 3 and Store 4. Since the balanced flow is assumed in the two heat exchangers and the effectiveness is unchanged during charging and discharging, the following equation is satisfied:

$$\Delta T_{\mathrm{c,1}} = \Delta T_{\mathrm{c,2}} = \Delta T_{\mathrm{c,3}} = \Delta T_{\mathrm{d,1}} = \Delta T_{\mathrm{d,2}} = \Delta T_{\mathrm{d,3}} \tag{A29}$$

Then the heat transfer rate, heat storage rate and heat release rate of the LSHS during charging and discharging are:

$$\dot{Q}_{\mathrm{tr,c,l}} = \dot{Q}_{\mathrm{st,c,l}} = \dot{m}_{\mathrm{f}}c_{\mathrm{p,f}}\left(T_{\mathrm{in,f,c}} - T_{\mathrm{out,f,c}}\right) \tag{A30}$$

$$\dot{Q}_{\mathrm{tr,d,l}} = \dot{Q}_{\mathrm{re,d,l}} = \dot{m}_{\mathrm{f}}c_{\mathrm{p,f}}\left(T_{\mathrm{out,f,d}} - T_{\mathrm{in,f,d}}\right) \tag{A31}$$

For the LSHS, the roundtrip efficiency (RTE) is defined as the thermal energy output divided by the thermal energy input to the store as follows:

$$\mathrm{RTE} = \frac{\int_0^\tau \dot{Q}_{\mathrm{re,d,l}}dt}{\int_0^\tau \dot{Q}_{\mathrm{st,c,l}}dt} \tag{A32}$$

The pressure loss on the tube side in LSHSs is calculated from Eq. (A22).

References

[1] BP, BP Energy Outlook, 2020. London.
[2] Y. Zhao, C.Y. Zhao, C.N. Markides, H. Wang, W. Li, Medium- and high-temperature latent and thermochemical heat storage using metals and metallic compounds as heat storage media: a technical review, Appl. Energy 280 (2020), 115950.
[3] A. Olympios, J. McTigue, P.F. Antunez, A. Tafone, A. Romagnoli, Y. Li, Y. Ding, W.-D. Steinmann, L. Wang, H. Chen, Progress and prospects of thermo-mechanical energy storage-a critical review, Prog. Energy 3 (2021), 022001.
[4] P. Blanc, M. Zafar, J. Levy, P. Gupta, Innovation Insights Brief-five Steps to Energy Storage, World Energy Council, London, 2020.
[5] A. Thess, Thermodynamic efficiency of pumped heat electricity storage, Phys. Rev. Lett. 111 (11) (2013), 110602.

[6] W.-D. Steinmann, Thermo-mechanical concepts for bulk energy storage, Renew. Sustain. Energy Rev. 75 (2017) 205–219.
[7] T.E.W. Schumann, Heat transfer: a liquid flowing through a porous prism, J. Franklin Inst. 208 (3) (1929) 405–416.
[8] T. Desrues, J. Ruer, P. Marty, J.F. Fourmigué, A thermal energy storage process for large scale electric applications, Appl. Therm. Eng. 30 (5) (2010) 425–432.
[9] A.J. White, Loss analysis of thermal reservoirs for electrical energy storage schemes, Appl. Energy 88 (11) (2011) 4150–4159.
[10] A. White, J. McTigue, C. Markides, Wave propagation and thermodynamic losses in packed-bed thermal reservoirs for energy storage, Appl. Energy 130 (2014) 648–657.
[11] A.J. White, J.D. McTigue, C.N. Markides, Analysis and optimisation of packed-bed thermal reservoirs for electricity storage applications, Proc.Inst.Mech.Eng.AJ. PowerEnergy 230 (7) (2016) 739–754.
[12] J.D. McTigue, C.N. Markides, A.J. White, Performance response of packed-bed thermal storage to cycle duration perturbations, J. Energy Storage 19 (2018) 379–392.
[13] J.D. McTigue, A.J. White, A comparison of radial-flow and axial-flow packed beds for thermal energy storage, Appl. Energy 227 (2018) 533–541.
[14] A. White, G. Parks, C.N. Markides, Thermodynamic analysis of pumped thermal electricity storage, Appl. Therm. Eng. 53 (2) (2013) 291–298.
[15] J.D. McTigue, A.J. White, C.N. Markides, Parametric studies and optimisation of pumped thermal electricity storage, Appl. Energy 137 (2015) 800–811.
[16] S. Georgiou, N. Shah, C.N. Markides, A thermo-economic analysis and comparison of pumped-thermal and liquid-air electricity storage systems, Appl. Energy 226 (2018) 1119–1133.
[17] S. Georgiou, M. Aunedi, G. Strbac, C.N. Markides, On the value of liquid-air and pumped-thermal electricity storage systems in low-carbon electricity systems, Energy 193 (2020), 116680.
[18] F. Ni, H.S. Caram, Analysis of pumped heat electricity storage process using exponential matrix solutions, Appl. Therm. Eng. 84 (2015) 34–44.
[19] A. Benato, Performance and cost evaluation of an innovative pumped thermal electricity storage power system, Energy 138 (2017) 419–436.
[20] A. Benato, A. Stoppato, Heat transfer fluid and material selection for an innovative pumped thermal electricity storage system, Energy 147 (2018) 155–168.
[21] S. Mumma, W. Marvin, A Method of Simulating the Performance of a Pebble Bed Thermal Energy Storage And Recovery System, American Society of Mechanical Engineers and American Institute of Chemical Engineers, 1976.
[22] L.X. Chen, P. Hu, P.P. Zhao, M.N. Xie, F.X. Wang, Thermodynamic analysis of a high temperature pumped thermal electricity storage (HT-PTES) integrated with a parallel organic Rankine cycle (ORC), Energy Convers. Manag. 177 (2018) 150–160.
[23] L. Wang, X. Lin, L. Chai, L. Peng, D. Yu, H. Chen, Cyclic transient behavior of the Joule-Brayton based pumped heat electricity storage: modeling and analysis, Renew. Sustain. Energy Rev. 111 (2019) 523–534.
[24] L. Wang, X. Lin, L. Chai, L. Peng, D. Yu, J. Liu, H. Chen, Unbalanced mass flow rate of packed bed thermal energy storage and its influence on the Joule-Brayton based pumped thermal electricity storage, Energy Convers.Manag. 185 (2019) 593–602.
[25] R.B. Laughlin, Pumped thermal grid storage with heat exchange, J.Renew.Sustain. Energy 9 (4) (2017), 044103.
[26] P. Farres-Antunez, H. Xue, A.J. White, Thermodynamic analysis and optimisation of a combined liquid air and pumped thermal energy storage cycle, J. Energy Storage 18 (2018) 90–102.
[27] Y. Zhao, M. Liu, J. Song, C. Wang, J. Yan, C.N. Markides, Advanced exergy analysis of a Joule-Brayton pumped thermal electricity storage system with liquid-phase storage, Energy Convers. Manag. 231 (2021), 113867.
[28] J. Howes, Concept and development of a pumped heat electricity storage device, Proc. IEEE (2011) 493–503.
[29] A. Smallbone, V. Jülch, R. Wardle, A.P. Roskilly, Levelised cost of storage for pumped heat energy storage in comparison with other energy storage technologies, Energy Convers.Manag. 152 (2017) 221–228.
[30] M. Saghafifar, M.A. Schnellmann, S.A. Scott, Chemical looping electricity storage, Appl. Energy 279 (2020), 115553.
[31] M. Saghafifar, S.A. Scott, The use of high decomposition temperature materials for chemical looping electricity storage, Chem. Eng. J. 423 (2021), 128789.
[32] Y.Q. Ge, Y. Zhao, C.Y. Zhao, Transient simulation and thermodynamic analysis of pumped thermal electricity storage based on packed-bed latent heat/cold stores, Renew.Energy 174 (2021) 939–951.
[33] H. Gadd, S. Werner, Achieving low return temperatures from district heating substations, Appl. Energy 136 (2014) 59–67.
[34] K. Thulukkanam, Heat Exchanger Design Handbook, 2nd ed., CRC Press, Florida, 2013.
[35] H. Michels, R. Pitz-Paal, Cascaded latent heat storage for parabolic trough solar power plants, Sol. Energy 81 (6) (2007) 829–837.
[36] E.W. Lemmon, M.L. Huber, M.O. McLinden, NIST Standard Reference Database 23: Reference Fluid Thermodynamic And Transport Properties-REFPROP, Version, 2013.
[37] T.L. Bergman, F.P. Incropera, D.P. DeWitt, A.S. Lavine, Fundamentals of Heat And Mass Transfer, 7th ed., John Wiley & Sons, New Jersey, 2011.
[38] N.H.S. Tay, M. Belusko, F. Bruno, An effectiveness-NTU technique for characterising tube-in-tank phase change thermal energy storage systems, Appl. Energy 91 (1) (2012) 309–319.
[39] PetroWiki, Pipeline Design Consideration And Standards, 2015.
[40] H.J. Xu, C.Y. Zhao, Thermal performance of cascaded thermal storage with phase-change materials (PCMs).Part I: steady cases, Int. J. Heat Mass Transf. 106 (2017) 932–944.
[41] R. Turton, R.C. Bailie, W.B. Whiting, J.A. Shaeiwitz, Analysis, Synthesis And Design of Chemical Processes, 4th ed., Pearson Education, New Jersey, 2012.
[42] M.W.J.E. Chase, NIST-JANAF Thermochemical Tables, J. Phys. Chem. Ref. Data, Monograph 9, 1998.
[43] J. Mo/lgaard, W.W. Smeltzer, Thermal conductivity of magnetite and hematite, J. Appl. Phys. 42 (9) (1971) 3644–3647.
[44] N. Wakao, T. Funazkri, Effect of fluid dispersion coefficients on particle-to-fluid mass transfer coefficients in packed beds, Chem. Eng. Sci. 33 (10) (1978) 1375–1384.
[45] S. Ergun, Fluid flow through packed columns, Chem. Eng. Prog. 48 (1952) 89–94.
[46] P.C. Carman, Fluid flow through granular beds, Chem. Eng. Res. Des. 75 (1997) S32–S48.
[47] H. Benoit, L. Spreafico, D. Gauthier, G. Flamant, Review of heat transfer fluids in tube-receivers used in concentrating solar thermal systems: properties and heat transfer coefficients, Renew. Sustain. Energy Rev. 55 (2016) 298–315.
[48] A. Modi, C.D. Pérez-Segarra, Thermocline thermal storage systems for concentrated solar power plants: one-dimensional numerical model and comparative analysis, Sol. Energy 100 (2014) 84–93.
[49] M. Liu, N.H. Steven Tay, S. Bell, M. Belusko, R. Jacob, G. Will, W. Saman, F. Bruno, Review on concentrating solar power plants and new developments in high temperature thermal energy storage technologies, Renew. Sustain. Energy Rev. 53 (2016) 1411–1432.
[50] G.-B. Wang, X.-R. Zhang, Thermodynamic analysis of a novel pumped thermal energy storage system utilizing ambient thermal energy and LNG cold energy, Energy Convers.Manag. 148 (2017) 1248–1264.